Principal Gaussian Overbound for Heavy-tailed Error Bounding

PENGGAO YAN
YIHAN ZHONG
LI-TA HSU, Senior Member, IEEE
Department of Aeronautical and Aviation Engineering, The Hong Kong Polytechnic University, Hong Kong

Abstract— A sharp yet conservative overbound for heavy-tailed error distributions is essential in integrity monitoring applications due to availability and continuity constraints. This paper proposes the Principal Gaussian overbound (PGO) for heavy-tailed error distributions by leveraging the characteristics of the Gaussian mixture model. The overbounding property of the PGO is proved to be preserved through convolution, which makes it possible to derive pseudorange-level requirements from the position domain integrity requirements. Experimental results on two datasets show that the PGO provides the most competitive bounding performance for heavy-tailed differential global navigation satellite system (DGNSS) pseudorange errors when compared to the two-step Gaussian overbound and Gaussian-Pareto overbound, yielding a sharp bound in both the core and tail parts of the error distribution. The proposed method reduces the mean vertical protection level (VPL) by more than 78% compared to the two-step Gaussian overbounding method on the urban dataset. In addition, the mean computation time of VPL is only $0.08\,\mathrm{s}$ with fifteen measurements by employing fast Fourier transforms, suggesting the substantial potential of the PGO in GNSS applications with strict integrity and real-time requirements. Furthermore, the feasibility of the PGO in fault detection is discussed.

Index Terms—Bounding methods, Gaussian mixture model, Heavy-tailed error distribution, Integrity analysis, Global navigation satellite system, Fast Fourier transforms

I. INTRODUCTION

Safety-of-life systems, such as satellite-based augmentation systems (SBAS), ground-based augmentation systems (GBAS), and receiver autonomous integrity monitoring (RAIM), have become increasingly important in modern aviation to ensure the safety and reliability of

Authors' address: The authors are with the Department of Aeronautical and Aviation Engineering, Faculty of Engineering, Hong Kong Polytechnic University, Hong Kong, E-mail: (peng-gao.yan@connect.polyu.hk; yihan1.zhong@connect.polyu.hk; lt.hsu@polyu.edu.hk).*(Corresponding author: Li-Ta Hsu.)*

navigation systems [1]–[3]. These systems are designed to provide integrity-assured position solutions to global navigation satellite system (GNSS) users and typically require a low integrity risk, which is the probability of a hazardously misleading information (HMI) event [4]. To achieve this, the position error distribution should be characterized to derive the protection level (PL), which serves as the maximum error bound applicable to the position solution to ensure that the integrity risk is below a specified threshold [5].

To meet the stringent navigation requirements, precise modeling of the error distribution using experimental data is essential, where the most challenging aspect of this task lies in accurately capturing and modeling the tail distribution [4], [6], [7]. Due to the relatively diminished probability of tail observations, a huge amount of data is needed to precisely characterize the tail distribution [7]. In addition, it is not a trivial task to account for heavy tails and other irregularities in the range error distribution, which may vary depending on satellite azimuth, satellite elevation, receiver hardware, terrain, and season [8]. To address this issue, a conservative representation of the error distribution known as the overbound is employed. The overbound represents the worst possible error distribution in the absence of a hardware fault [8], [9]. In general, there are three constraints on overbounding. The first constraint originates from the integrity requirement in the position domain. The overbound of the positioning error, which is derived from the overbounds on the range-domain error, should have a larger probability beyond the PL than the actual positioning error, indicating the conservative of the overbound in both the range and position domains [8]. Second, a sharp overbound that closely resembles the shape of the actual error distribution while remaining conservative is favored due to the availability and continuity constraints [8]. Finally, a simple, parameterized form of the overbound is essential to support limited-bandwidth communication and rapid PL computation [10].

The first true overbound, known as the cumulative distribution function (CDF) overbound, was introduced by DeCleene in 2000 [9]. It is defined as having more tail mass than the error distribution. To facilitate the range-to-position projection and simplify the communication and computation of error bounds, the zero-mean Gaussian model is adopted as the underly form of the CDF overbound. Since then, the Gaussian CDF overbound and its variants have dominated the overbounding research and are taken as the basis for integrity analysis. Nevertheless, DeCleene's method requires certain shape constraints on the overbounding distribution, including symmetric and unimodality. To relax these constraints, Rife et al. proposed the paired CDF overbound that uses two Gaussian distributions with non-zero mean to overbound the left and right regions separately [11]. However, its stringent requirement on bounding both regions inflates the standard deviation or enlarges the biases in the Gaussian overbound [10]. This problem is relieved by allowing the

total mass of the overbound distribution to be greater than one, which is known as the excess-mass CDF (EMC) overbound [5]. More recently, Blanch et al. proposed the two-step Gaussian overbounding method, significantly reducing the bias in the overbound distribution [10]. Nonetheless, these Gaussian-based overbounding methods fail to truly overbound the heavy-tailed distributions, a frequent occurrence in pseudorange errors influenced by multipath [7]. This is because heavy-tailed distributions have tails that are not exponentially bounded, which makes them impossible to be overbounded by a Gaussian distribution that only possesses an exponential tail [4], [8]. It is natural to apply different models for the core and tail regions of a distribution. Rife et al. proposed the Gaussian core overbound, which utilizes a Gaussian distribution for the core bounding and an implicit distribution for the tail bounding [8]. More recently, Larson et al. proposed the Gaussian-Pareto overbound to tightly bound the tails by utilizing the extreme value theory [4]. However, the overbounding property of the Gaussian-Pareto overbound through convolution remains unclear, which currently limits its applications.

In addition to Gaussian or semi-Gaussian overbounding methods, researchers have developed non-Gaussian overbounding methods by exploiting the properties of non-Gaussian models in modeling heavy-tailed distributions [12]–[14]. For example, Xue et al. utilized the stable distribution to model the GBAS ranging error and derived the analytical equation of PLs [14]. Blanch et al. constructed a bimodal Gaussian mixture model for modeling the pseudorange error in the worst case and presented the numerical method for the range-to-position projection [12]. Rife et al. proposed the Gaussian Core Gaussian Sidelobes (GCGS) bound, which uses several equal-variance Gaussian components to model the heavy tails of the error distribution [8]. Although the GCGS bound is formalized as the convolution of a single Gaussian distribution with a set of delta functions, the GCGS bound is indeed a GMM. Gao et al. also utilized the Gaussian mixture model to characterize the ionosphere free based range errors of GBAS [15]. Although these methods have shown great potential in tightly bounding heavy-tailed distributions, the parameters of the non-Gaussian distribution are identified either through worst-case analysis or sample fitting. These approaches cannot rigorously determine the least conservative overbound of the error distribution.

In this work, we propose the Principal Gaussian overbound (PGO) for heavy-tailed error distribution based on the Gaussian mixture model. Specifically, the bimodal Gaussian mixture model (BGMM) is employed to fit the error distribution based on the expectation-maximization algorithm [16]. A partition strategy based on the analysis of BGMM membership weight is proposed, which divides the BGMM into the core and tail regions. Within each region, one of the Gaussian components in the BGMM holds a dominant position, and a CDF overbound is constructed based on the dominant Gaussian component.

The PGO is named based on the nature of the overbounding process. A sigma inflation strategy is further proposed to compensate the PGO, which allows it to bound the sample distribution as well as the fitted BGMM. The overbound property of the PGO is proved to be preserved through convolution. In addition, the position-domain bounding and the PL are calculated based on the fast Fourier transform [17], which largely reduces the computation load compared to the direct convolution approach. The bounding performance of the proposed PGO is evaluated on two differential global navigation satellite system (DGNSS) pseudorange datasets, including the DGNSS pseudorange data collected from two Continuously Operating Reference Stations (CORS) in Minneapolis and the DGNSS pseudorange data collected from a slightly urbanized area in Hong Kong. Results show that the PGO can provide a sharper bound on heavy-tailed error distributions compared to the two-step Gaussian overbound [10] and yield competitive bounding performance compared to the Gaussian-Pareto overbound [4]. In addition, compared to the two-step Gaussian overbounding method, the proposed method reduces the mean vertical protection level (VPL) by more than $78\,\%$ without compromising integrity on the urban dataset. The mean computation time of VPL is only $0.08\,\mathrm{s}$ with fifteen measurements, which is well acceptable for a personal computer. The contributions of this study are two folds:

1) Propose a CDF overbound (Principal Gaussian overbound) for heavy-tailed error distributions and prove that its overbounding property can be preserved through convolution. The calculation of PLs is formalized based on the fast Fourier transform, which largely reduces the computation time.
2) Experimentally demonstrate the bounding performance of the proposed method in both range and position domains with CORS and urban DGNSS datasets. Especially in the urban dataset, PGO reduces the mean VPL by over $78\,\%$ without compromising integrity when compared to the two-step Gaussian overbounding method.

The rest of this article is organized as follows. Section II gives a brief review of the Gaussian overbounding methods, which are classified into two categories, including the paired overbounding methods and the core overbounding methods. The paired CDF overbound, EMC overbound, two-step Gaussian overbound, core overbound, and the Gaussian-Pareto overbound are reviewed. In Section III, the GMM and its application on error fitting and overbounding research are illustrated, which provides the theoretical foundation for the development of PGO in Section IV. In addition, the preservation of overbounding property through convolution and the position-domain bounding are illustrated in Section IV.D and Section IV.E, respectively. Section V compares the bounding performance of the PGO with the two-step Gaussian overbound and the Gaussian-Pareto overbound. In Section VI.A, the impact of the partition parameter on the bounding performance

of the PGO is discussed. Section VI.C forecasts the application of the PGO in fault detection tasks. Finally, Section VII presents a summary.

II. OVERVIEW OF GAUSSIAN OVERBOUNDING METHODS

Gaussian overbounding methods have played vital roles in overbounding research, mainly attributed to their simplicity and the preservation of their overbounding properties through convolution. Researchers are devoted to deriving a tight overbound of the error distribution and propose various overbounding methods, such as paired CDF overbound [11], two-step Gaussian overbound [10], and Gaussian-Pareto overbound [4]. These methods, although diverse in their application, share a common logic and can be methodically classified into two categories: paired overbounding methods and core overbounding methods. In this section, we use the random variable v to represent error and ov to represent the random variable related to the overbound distribution of v.

A. Paired Overbounding Methods

1. Paired CDF overbound

In the paired CDF overbounding method [11], the CDF of the overbound ($G_{ov}(x)$) is constructed by two CDFs, i.e., $G_L(x)$ and $G_R(x)$, as follows:

$$G_{ov}(x) = \begin{cases} G_L(x) & \forall G_L < \frac{1}{2} \\ G_R(x) & \forall G_R > \frac{1}{2} \\ \frac{1}{2} & \text{otherwise} \end{cases} \tag{1}$$

$G_L(x)$ and $G_R(x)$ can take any form as long as they are CDFs. However, the distribution of v is said to be paired CDF overbounded by $G_{ov}(x)$ only if

$$G_v(x) \le G_L(x) \ \forall x \tag{2a}$$
$$G_v(x) \ge G_R(x) \ \forall x, \tag{2b}$$

where $G_v(x)$ is the CDF of v. In the case of Gaussian paired overbound [11], $G_L(x)$ and $G_R(x)$ are the CDF of a Gaussian distribution taking the form:

$$G_L(x) = \int_{-\infty}^{x} f_N(x; -b_L, \sigma_L) \, dx \tag{3a}$$

$$G_R(x) = \int_{-\infty}^{x} f_N(x; b_R, \sigma_R) \, dx, \tag{3b}$$

where $f_N(x; b_*, \sigma_*)$ is the probability density function (PDF) of a Gaussian distribution with mean b_* and standard deviation σ_* as follows:

$$f_N(x; b_*, \sigma_*) = \frac{1}{\sigma_* \sqrt{2\pi}} \exp \frac{-(x - b_*)^2}{2\sigma_*^2}. \tag{4}$$

By letting $b_L = b_R > 0$ and $\sigma_L = \sigma_R$, Rife et al. formulated a symmetric paired Gaussian overbound for the Wide Area Augmentation System (WAAS) and the Local Area Augmentation System (LAAS) applications [11]. This method, due to its significant advantage of not introducing new parameters into the broadcast signal

of both augmentation systems, has been widely adopted. However, the stringent requirement in (2) would extensively inflate the standard deviation or enlarge the biases in the Gaussian overbound [10].

2. EMC overbound

To tackle the issue of the flattened standard deviation, Rife et al. proposed the excess-mass CDF (EMC) overbound [5] by allowing the total mass of the overbound distribution greater than one. The Gaussian EMC overbound can be constructed by introducing the total mass parameter $K > 1$ into (3), which is expressed as

$$G_L^*(x) = \int_{-\infty}^{x} K \cdot f_N(x; -b_L, \sigma_L) \, dx \tag{5a}$$

$$G_R^*(x) = \int_{-\infty}^{x} K \cdot f_N(x; b_R, \sigma_R) \, dx + (1 - K). \tag{5b}$$

The total mass parameter K provides an extra degree of freedom (DOF) for the sharp bounding of the error distribution. However, the Gaussian EMC overbound is a generalization of the paired CDF overbound and still needs to bound the CDF of the error distribution for all values (as required in (2)), which inevitably requires large biases in the overbound distribution [10].

3. Two-step Gaussian overbound

The large bias problem is improved by the two-step Gaussian overbounding method [10], which relaxes the constraints in (2) by employing an intermediate overbound distribution. In the first step, a piecewise uniform, symmetric, and unimodal distribution $G_{su}(x)$ is determined through an ad hoc approach:

$$G_v(x) \le G_{su}(x) \ \forall x. \tag{6}$$

In the second step, the left-hand side overbound is determined by finding the minimum σ_L that satisfies

$$\int_{-\infty}^{x} f_N(x; -b_L, \sigma_L) \, dx \ge G_{su}(x) \ \forall x \le 0. \tag{7}$$

Equation (7) relaxes the constraint in (2), i.e., only the left-hand side of the intermediate distribution needed to be CDF overbounded. The right-hand side overbound is obtained by repeating the above process on the mirror image of the sample distribution, i.e., $G_v(-x)$. The right-hand side overbound has the CDF form as follows:

$$\int_{-\infty}^{x} f_N(x; b_R, \sigma_R) \, dx \ \forall x > 0. \tag{8}$$

Although the two-step Gaussian overbounding method can significantly reduce the bias compared to the conventional paired overbounding methods [10], its overbound for the heavy-tailed distribution can still be conservative, which will be shown through numerical experiments in Section V.

B. Core Overbounding Methods

1. Core overbound

The core overbounding concept [8] is proposed to tackle tail uncertainty by adding a small probability at

infinity, which closely resembles DeCleene's theorem that the pseudorange error has to be bounded to infinity [9]. Specifically, this concept decomposes the error distribution into two fractions, including the core part $G_{v,\text{core}}(x)$ and the tail part $G_{v,\text{tail}}(x)$ as follows,

$$G_v(x) = G_{v,\text{core}}(x) + G_{v,\text{tail}}(x), \quad (9)$$

where $G_{v,\text{core}}(x)$ and $G_{v,\text{tail}}(x)$ are defined in terms of the error distribution PDF $f_v(x)$ as follows:

$$G_{v,\text{core}}(x) = \begin{cases} \int_{-\infty}^x f_v(x)\,\mathrm{d}x & |x| \le T \\ 0 & |x| > T \end{cases} \quad (10a)$$

$$G_{v,\text{tail}}(x) = \begin{cases} 0 & |x| \le T \\ \int_{-\infty}^x f_v(x)\,\mathrm{d}x & |x| > T \end{cases}, \quad (10b)$$

where T is the core-tail transition point. The core overbound of $G_v(x)$ is defined as

$$G_{ov}(x) = \hat{G}_{ov,\text{ex}}(x) + \hat{G}_{ov,\text{im}}(x), \quad (11)$$

where $\hat{G}_{ov,\text{ex}}(x)$ and $\hat{G}_{ov,\text{im}}(x)$ are CDFs scaled by a factor within the range of zero to one. In general, $\hat{G}_{ov,\text{ex}}(x)$ is an explicit function that bounds the worse-case CDF of the core part of the error distribution,

$$G_{v,\text{core}}(x) \le \hat{G}_{ov,\text{ex}}(x) \ \forall -T \le x \le 0 \quad (12a)$$

$$G_{v,\text{core}}(x) \ge \hat{G}_{ov,\text{ex}}(x) \ \forall 0 < x \le T, \quad (12b)$$

and $G_{ov,\text{im}}(x)$ is an implicit function (i.e., no assumptions are made on its shape) that bounds the tail part of the error distribution,

$$G_{v,\text{tail}}(x) \le \hat{G}_{ov,\text{im}}(x) \ \forall x < -T \quad (13a)$$

$$G_{v,\text{tail}}(x) \ge \hat{G}_{ov,\text{im}}(x) \ \forall x > T. \quad (13b)$$

As a realization of the core overbounding concept, the Gaussian Core (GC) overbound is proposed in the same paper [8] as follows:

$$\hat{G}_{\text{GC,ex}}(x) = (1 - P_t)\, f_N(x; 0, \sigma_0) \quad (14a)$$

$$\hat{G}_{\text{GC,im}}(x) = \frac{1}{2} P_t, \quad (14b)$$

where σ_0 is the standard deviation of the Gaussian core, and P_t is the total probability of the tail error,

$$P_t = G_{v,\text{tail}}(T). \quad (15)$$

It is clear that the tightness of the overbound in the tail region depends on the magnitude of P_t. If the Gaussian core can bound the most part of the error distribution, P_t can take extremely small values. However, this comes with the sacrifice of increasing σ_0, especially when bounding heavy-tailed error distributions.

2. Gaussian-Pareto overbound

Instead of employing the implicit tail core, Larson et al. proposed the Gaussian-Pareto overbound [4] by adopting the generalized Pareto distribution for the tails. The Gaussian-Pareto overbound stems from the extreme value theory, which shows that almost all normalized continuous probability distributions asymptotically approach a generalized Pareto distribution [18]. This property enables the generalized Pareto distribution to provide a true

overbound for data far beyond the end of the empirical distributions, as required in DeCleene's theorem [9]. The tail of the Gaussian-Pareto overbound can be formalized as

$$\hat{G}_{\text{GP,tail}}(x)$$
$$= \begin{cases} G_v(u_L) - G_{\text{GPD}}(u_L - x)\, G_v(u_L) & \forall x < u_L \\ G_{\text{GPD}}(x - u_R)(1 - G_v(u_R)) + G_v(u_R) & \forall x > u_R \end{cases}, \quad (16)$$

where $u_L < 0$ is the left core-tail transition point, $u_R > 0$ is the right core-tail transition point, and $G_{\text{GPD}}(x; \mu, \beta, \gamma)$ is the CDF of the generalized Pareto distribution with a location parameter, u, a scale parameter, β, and a shape parameter, γ [19], as shown below:

$$G_{\text{GPD}}(x; u, \beta, \gamma) = \begin{cases} 1 - \left(1 + \frac{\gamma(x-u)}{\beta}\right)^{-\frac{1}{\gamma}} & \gamma \ne 0 \\ 1 - \exp\left(-\frac{x-u}{\beta}\right) & \gamma = 0 \end{cases}. \quad (17)$$

Although the Gaussian-Pareto overbounding method offers the potential to tightly overbound the tail distribution, it is unclear whether the Gaussian-Pareto overbound can maintain the overbounding property through convolution, which is crucial for deriving pseudorange-level requirements from the position-domain integrity requirement [9].

III. GAUSSIAN MIXTURE MODEL

GMM is a statistical technique that plays a crucial role in error modeling, particularly in capturing heavy-tailed distributions that are commonly observed in real-world scenarios [12], [20], [21]. A GMM represents a probability distribution as a weighted combination of multiple Gaussian distributions, each representing a component of the mixture. In particular, BGMM is of significant research interest as it effectively balances simplicity and flexibility, enabling precise modeling of both the core and tails of heavy-tailed distributions while avoiding overfitting and excessive parameters [12], [22]. The PDF of a zero-mean BGMM for heavy-tailed distribution modeling can be formalized as

$$f(x) = p_1 f_N(x; 0, \sigma_1) + (1 - p_1) f_N(x; 0, \sigma_2), \quad (18)$$

where $f_N(x; 0, \sigma_1)$ and $f_N(x; 0, \sigma_2)$ are the PDF of the first and the second Gaussian component, σ_1 and σ_2 are the corresponding standard deviations, and p_1 and $1 - p_1$ are the mixing weight of the two Gaussian components, respectively. In this paper, it is assumed that $\sigma_1 < \sigma_2$ and $p_1 \in (0.5, 1)$, indicating that the Gaussian component with the smaller standard deviation is selected as the 1st Gaussian component and exhibits a higher mixing weight. The estimation of parameters in a GMM can be accomplished through Maximum Likelihood Estimation (MLE). The expectation-maximization (EM) algorithm [16] is usually adopted to obtain the MLE. A concise summary of the EM algorithm is provided in Appendix A.

Due to the appealing nature of GMM, research on GMM-based overbounds emerged as early as 2001 and

has received increased attention in recent years [7]. Shively compared GMM overbounding methods with Gaussian and exponential overbounding methods in terms of the resulting inflation factor, suggesting that the GMM method may align most closely with the manner in which errors are present in actual data [7]. Lee used the GMM as an empirical distribution to model the ground facility error distribution, showing the potential of GMM to reduce the inflation factor and the PL [22]. However, the PL is calculated by a Gaussian overbound of the GMM, which inevitably increases the conservatism. To tackle this issue, Blanch et al. constructed a BGMM for pseudorange error modeling in the worst case [12]. They proved that the posterior position density is also GMM and derived the PL by integrating the posterior position density. Nevertheless, the computation of the PL involves a large number of matrix inversions, which cause a considerable computation burden.

These studies usually obtain the GMM from the worst-case analysis [12] or sample data fitting [15], [16]. However, a rigorous method to determine the least conservative GMM overbound of the error distribution has not been developed. The crux of this issue lies in the difficulty of establishing overbounding relationships between two GMMs. In Gaussian scenarios, a Gaussian with a larger standard deviation can always bound the Gaussian with a smaller standard deviation. However, in the context of GMMs, the increasing parameters can provide more flexibility in shaping the distribution, which in turn makes it more difficult to assess whether one GMM's distribution covers the entire range of the other GMM's distribution. Therefore, this paper explores an alternative way to utilize GMM to bound the heavy-tailed error distribution. We propose the PGO, which is proven to be the true CDF overbound of the GMM distribution.

IV. PRINCIPAL GAUSSIAN OVERBOUND FOR THE HEAVY-TAILED ERROR DISTRIBUTION

A. Membership Weight Analysis

The process of generating samples from a GMM can be seen as simultaneously generating samples from multiple Gaussian distributions according to their respective weights. For example, given a K-component GMM with mixture weights of p_1, p_2,..., p_K, the sample generated from it at time t is drawn from the 1st component with probability p_1, drawn from the 2nd component with probability p_2, and etc. From the perspective of statistical inference, we can also estimate the likelihood of a sample belonging to a specific Gaussian component, which is known as the membership weight. The membership weight indicates the posterior probability of a data point being generated from each component, which can be derived by utilizing the Bayes' Theorem [23]. For a given observation x, we define the allocation variable $c = \{1, 2, \ldots, K\}$ that marks the Gaussian component from which x is generated. Then, the mixture weight of

the kth Gaussian component can be interpreted as the prior probability of the allocation variable that equals k, as shown below:

$$p_k = P\left(c = k\right). \tag{19}$$

For a given $c = k$, the probability of generating x (i.e., the likelihood) is

$$P\left(x|c = k\right) = f_N\left(x; b_k, \sigma_k\right). \tag{20}$$

According to Bayes' Theorem, the posterior probability is given by

$$s_k = P\left(c = k|x\right) = \frac{p_k f_N\left(x; b_k, \sigma_k\right)}{\sum_{k=1}^{K} p_k f_N\left(x; b_k, \sigma_k\right)}, \tag{21}$$

where s_k is the membership weight of the kth Gaussian component for the observation x.

In this paper, we mainly focus on the zero-mean BGMM in (18) due to its good balance of simplicity and flexibility. The membership weights s_1 and s_2 of the zero-mean BGMM can be written as

$$s_1(x) = \frac{p_1 f_N\left(x; 0, \sigma_1\right)}{p_1 f_N\left(x; 0, \sigma_1\right) + \left(1 - p_1\right) f_N\left(x; 0, \sigma_2\right)} \tag{22a}$$

$$s_2(x) = \frac{\left(1 - p_1\right) f_N\left(x; 0, \sigma_2\right)}{p_1 f_N\left(x; 0, \sigma_1\right) + \left(1 - p_1\right) f_N\left(x; 0, \sigma_2\right)}$$

$$= 1 - s_1(x). \tag{22b}$$

By substituting the PDF equation of a Gaussian distribution into (22a),

$$s_1(x) = \frac{\frac{p_1}{\sigma_1} \exp\left(-\frac{1}{2}\left(\frac{x}{\sigma_1}\right)^2\right)}{\frac{p_1}{\sigma_1} \exp\left(-\frac{1}{2}\left(\frac{x}{\sigma_1}\right)^2\right) + \frac{1-p_1}{\sigma_2} \exp\left(-\frac{1}{2}\left(\frac{x}{\sigma_2}\right)^2\right)}$$

$$= \frac{1}{1 + \frac{1-p_1}{p_1}\frac{\sigma_1}{\sigma_2} \exp\left(\frac{\sigma_2^2 - \sigma_1^2}{2\sigma_1^2 \sigma_2^2} x^2\right)}. \tag{23}$$

Since $\sigma_2 > \sigma_1$, $\exp\left(\frac{\sigma_2^2 - \sigma_1^2}{2\sigma_1^2 \sigma_2^2} x^2\right)$ will be a symmetric convex function in terms of x; Hence, $s_1(x)$ will be a symmetric concave function. Since $s_2(x) = 1 - s_1(x)$, $s_2(x)$ will consequently be a symmetric convex function. Fig. 1 plots $s_1(x)$ and $s_2(x)$ in two settings of GMMs, including $p_1 = 0.9, \sigma_1 = 0.5, \sigma_2 = 0.7$ in Fig. 1a and $p_1 = 0.9, \sigma_1 = 0.5, \sigma_2 = 1.5$ in Fig. 1c. In both cases, $s_1(x)$ has large values when x is located at the central region of the BGMM, and the value decreases dramatically when x goes far away from the center. However, $s_2(x)$ shows an opposite trend that the largest value of $s_2(x)$ is located at the tail region. These trends indicate the dominance of each Gaussian component in different regions of the BGMM, which provides the theoretical foundation for the dominance partition illustrated in the next section.

B. Dominance Partition

It is straightforward to use the intersection points of $s_1(x)$ and $s_2(x)$ to partition the core and tail regions of
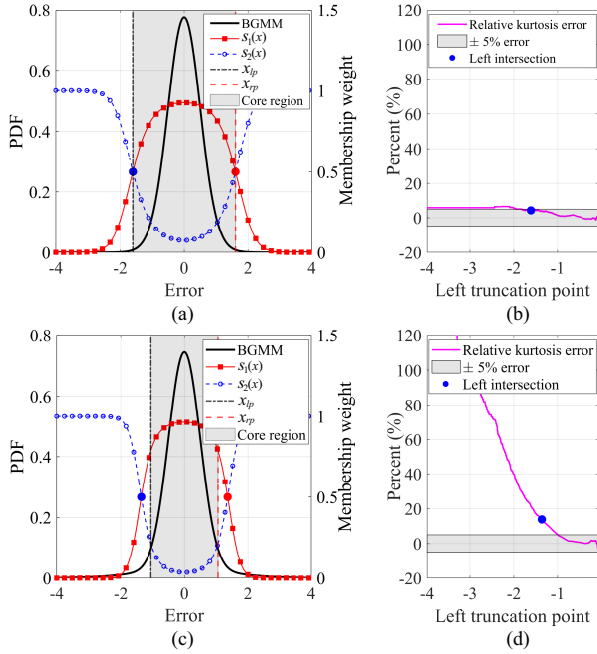
Fig. 1. (a) Membership weights and (b) the relative kurtosis error of a zero-mean BGMM with $p_1 = 0.9$, $\sigma_1 = 0.5$, and $\sigma_2 = 0.7$; (c) Membership weights and (d) the relative kurtosis error of a zero-mean BGMM with $p_1 = 0.9$, $\sigma_1 = 0.5$, and $\sigma_2 = 1.5$. x_{lp} and x_{rp} are the core-tail transition points. The two intersection points of $s_1(x)$ and $s_2(x)$ are marked with blue and red solid points.

the zero-mean BGMM. The intersection points $x_{\text{intersect}}^{\text{L}}$ and $x_{\text{intersect}}^{\text{R}}$ can be found by solving $s_1(x) = s_2(x)$ as

$$x_{\text{intersect}}^{\text{L}} = -\sqrt{\frac{2\sigma_1^2\sigma_2^2}{\sigma_2^2 - \sigma_1^2}\ln\frac{p_1\sigma_2}{(1-p_1)\,\sigma_1}} \quad (24a)$$

$$x_{\text{intersect}}^{\text{R}} = \sqrt{\frac{2\sigma_1^2\sigma_2^2}{\sigma_2^2 - \sigma_1^2}\ln\frac{p_1\sigma_2}{(1-p_1)\,\sigma_1}} . \quad (24b)$$

According to the convex property of $s_2(x)$, the value of $s_2(x)$ will exceed 0.5 and increase monotonically as the data point moves away from $x_{\text{intersect}}^{\text{R}}$ to ∞ (or from $x_{\text{intersect}}^{\text{L}}$ to $-\infty$). Meanwhile, $s_1(x)$ will decrease monotonically and eventually go to zero. This trend indicates that the 2nd Gaussian component dominants the region $x \in \left(-\infty, x_{\text{intersect}}^{\text{L}}\right] \cup \left[x_{\text{intersect}}^{\text{R}}, \infty\right)$.

However, the dominance relationship in the region $x \in \left[x_{\text{intersect}}^{\text{L}}, x_{\text{intersect}}^{\text{R}}\right]$ is more complicated than that in the region $x \in \left(-\infty, x_{\text{intersect}}^{\text{L}}\right] \cup \left[x_{\text{intersect}}^{\text{R}}, \infty\right)$. Although $s_2(x)$ monotonically decreases when x gradually moves to the center, $s_2(x)$ will not be reduced to zero, which indicates that the impacts of the 2nd Gaussian component in the region $x \in \left[x_{\text{intersect}}^{\text{L}}, x_{\text{intersect}}^{\text{R}}\right]$ cannot be ignored. To quantify the impacts of the 2nd Gaussian component on the tailedness of the BGMM distribution, we calculate the kurtosis, a measure of tailedness, of the doubly truncated zero-mean BGMM and compare it with the kurtosis of doubly truncated standard normal distribution [24], [25]. Specifically, we randomly generate $N_t = 10,000$ samples from the zero-mean BGMM and truncate samples smaller than x_t^{L} or larger than x_t^{R}, where $x_t^{\text{L}} < 0$ and $x_t^{\text{R}} > 0$ are

the truncation points. The truncation rate γ_t is defined by

$$\gamma_t = 1 - \frac{n_t}{N_t}, \quad (25)$$

where n_t is the number of samples in $[x_t^{\text{L}}, x_t^{\text{R}}]$. Then we calculate the kurtosis of samples within $[x_t^{\text{L}}, x_t^{\text{R}}]$ by

$$k_{\text{BGMM}}(x_t^{\text{L}}) = \frac{\frac{1}{n_t}\sum_{x_i \in [x_t^L, x_t^R]}(x_i - \bar{x})^4}{\left[\frac{1}{n_t}\sum_{x_i \in [x_t^L, x_t^R]}(x_i - \bar{x})^2\right]^2}, \quad (26)$$

where $\bar{x}$ is the mean of samples within $[x_t^{\text{L}}, x_t^{\text{R}}]$. The corresponding truncation points of the standard normal distribution can be calculated by

$$x_{\text{normal}}^{\text{L}} = Q^{-1}\left(\frac{\gamma_t}{2}\right)$$
$$x_{\text{normal}}^{\text{R}} = -x_{\text{normal}}^{\text{L}}, \quad (27)$$

where $Q^{-1}(\cdot)$ is the quantile function of the standard normal distribution. (27) ensures that the doubly truncated standard normal distribution has the same truncation rate as the doubly truncated zero-mean BGMM. Similarly, we generate $N_t = 10,000$ samples from the standard normal distribution and calculate the kurtosis of the truncated distribution by setting $x_{\text{normal}}^{\text{L}}$ and $x_{\text{normal}}^{\text{R}}$ as the truncation points. The kurtosis of the doubly truncated standard normal distribution is denoted as $k_{\text{normal}}(x_t^{\text{L}})$. We then calculate the relative error between $k_{\text{BGMM}}(x_t^{\text{L}})$ and $k_{\text{normal}}(x_t^{\text{L}})$ by

$$e_k(x_t^{\text{L}}) = \frac{k_{\text{BGMM}}(x_t^{\text{L}}) - k_{\text{normal}}(x_t^{\text{L}})}{k_{\text{normal}}(x_t^{\text{L}})}, \quad (28)$$

and plot its value against x_t^{L} in Fig. 1.

Fig. 1b shows the relative kurtosis error in the case of BGMM with $p_1 = 0.9$, $\sigma_1 = 0.5$, and $\sigma_2 = 0.7$. The relative kurtosis error is within the $\pm 5\,\%$ error region when $x_t^{\text{L}} \geq x_{\text{intersect}}^{\text{L}}$, indicating that samples in the core region $x \in \left[x_{\text{intersect}}^{\text{L}}, x_{\text{intersect}}^{\text{R}}\right]$ show similar tailedness with the truncated standard normal distribution. This indicates that $x_{\text{intersect}}^{\text{L}}$ could be a good core-tail transition point since the core region $x \in \left[x_{\text{intersect}}^{\text{L}}, x_{\text{intersect}}^{\text{R}}\right]$ is less affected by the 2nd Gaussian component. However, the situation becomes different in the case of BGMM with $p_1 = 0.9$, $\sigma_1 = 0.5$, and $\sigma_2 = 1.5$, as shown in Fig. 1d. The relative kurtosis error is $14\,\%$ when $x_t^{\text{L}} = x_{\text{intersect}}^{\text{L}} = -1.36$, and this value slowly decreases to $5\,\%$ until x_t^{L} increases to -1. If we adopt $x_{\text{intersect}}^{\text{L}}$ as the core-tail transition point, the core region could be severely affected by the 2nd Gaussian component, making it difficult to distinguish the dominance relationship in the core region. Therefore, it is more beneficial to use the truncation point with $5\,\%$ relative kurtosis error as the core-tail transition point. In summary, we use the following rules to choose the core-tail transition point

$$x_{lp} = \begin{cases} x_{\text{intersect}}^{\text{L}} & \text{if } |e_k(x_{\text{intersect}}^{\text{L}})| \leq \alpha \\ x_t^{\text{L}} \text{ s.t. } e_k(x_t^{\text{L}}) = \alpha & \text{if } |e_k(x_{\text{intersect}}^{\text{L}})| > \alpha \end{cases}, \quad (29)$$

$$x_{rp} = -x_{lp}, \quad (30)$$

where α is the partition parameter. We define $[x_{lp}, x_{rp}]$ as the core region and $(-\infty, x_{lp}) \cup (x_{rp}, \infty)$ as the tail

region. In this paper, we choose $\alpha = 0.05$. Section VI.A will discuss the impacts of the partition parameter α on the bounding performance of the PGO.

C. Principal Gaussian Overbound

In this section, we propose the PGO based on the scaling and shifting of the dominant Gaussian component of the BGMM in the tail and core regions. The PDF of the PGO takes the following form:

$$f_o(x) = \begin{cases} (1+k)(1-p_1) f_N(x;0,\sigma_2) & |x| > x_{rp} \\ p_1 f_N(x;0,\sigma_1) + c & |x| \le x_{rp} \end{cases}, \tag{31}$$

where k is the scaling parameter, and c is the shifting parameter. The remainder of this section illustrates the construction of PGO.

1. Tail region bounding

In the tail region, the BGMM is dominated by the 2nd Gaussian component. Therefore, the 2nd Gaussian component, along with its mixture weight, is taken as the basis for bounding the tail region. In addition, compensation is needed to account for the contribution of the 1st component in the tail region. An intuitive approach of the CDF overbound at the left tail region is shown as follows:

$$\begin{aligned} G_o^{\mathrm{L}}(x) = {} & p_1 G(x_{lp};0,\sigma_1) \\ & + (1-p_1) G(x;0,\sigma_2) \ \ \forall x < x_{lp}, \end{aligned} \tag{32}$$

where $G(x;0,\sigma_1)$ and $G(x;0,\sigma_2)$ are the CDF of the 1st and 2nd Gaussian component, respectively. Let $G(x)$ be the CDF of the BGMM defined in (18),

$$\begin{aligned} G_o^{\mathrm{L}}(x) - G(x) = {} & G_o^{\mathrm{L}}(x) - \big(p_1 G(x;0,\sigma_1) \\ & + (1-p_1) G(x;0,\sigma_2)\big) \\ = {} & p_1\big(G(x_{lp};0,\sigma_1) - G(x;0,\sigma_1)\big). \end{aligned} \tag{33}$$

Since $x < x_{lp}$, we have $G(x_{lp};0,\sigma_1) - G(x;0,\sigma_1) > 0$. Therefore, $G_o^{\mathrm{L}}(x)$ is the CDF overbound of the BGMM at the left tail region. However, the CDF overbound in (32) includes a constant term, $p_1 G(x_{lp};0,\sigma_1)$, which is defined in an unbounded interval. This poses a challenge in deriving the PDF of the overbound distribution, which is necessary for convolution purposes.

We notice that $p_1 G(x_{lp};0,\sigma_1)$ in (32) is a constant term, which could be compensated by inflating the weight of the 1st Gaussian component, i.e., $G(x;0,\sigma_2)$ in (32). Therefore, we introduce the scaling parameter k into (32) as follows:

$$G_o^{\mathrm{L}}(x) = (1+k)(1-p_1) G(x;0,\sigma_2) \ \ \forall x < x_{lp}. \tag{34}$$

We need to determine the value of k so that (34) is a CDF overbound. Let (32) and (34) produce the same value at x_{lp}, the value of k can be determined by

$$k = \frac{p_1 G(x_{lp};0,\sigma_1)}{(1-p_1) G(x_{lp};0,\sigma_2)}. \tag{35}$$

Appendix B gives proof that $G_o^{\mathrm{L}}(x)$ in (34) is the CDF overbound at the left tail region. The PDF of the overbound distribution at the left tail region can be derived

by taking the derivative of (34) as

$$f_o^{\mathrm{L}}(x) = (1+k)(1-p_1) f_N(x;0,\sigma_2) \ \ \forall x < x_{lp}. \tag{36}$$

Similarly, the PDF of the overbound distribution at the right tail region can be written as

$$f_o^{\mathrm{R}}(x) = (1+k)(1-p_1) f_N(x;0,\sigma_2) \ \ \forall x > x_{rp}. \tag{37}$$

2. Core region bounding

In the core region, the BGMM is dominated by the 1st Gaussian component, as illustrated in Section IV.B. Nevertheless, the contribution of the 2nd Gaussian component to the probability distribution in the core region is not negligible. Therefore, we introduce a constant term c to compensate for such a contribution when developing the overbound distribution in the core region, as shown below:

$$f_o^{\mathrm{core}}(x) = p_1 f_N(x;0,\sigma_1) + c \ \ \forall x_{lp} \le x \le x_{rp}, \tag{38}$$

To determine the value of c, we calculate the CDF of $f_o^{\mathrm{core}}(x)$ through integration as follows:

$$\begin{aligned} G_o^{\mathrm{core}}(x) = {} & \int_{-\infty}^{x_{lp}} f_o^{\mathrm{L}}(x)\,\mathrm{d}x + \int_{x_{lp}}^{x} f_o^{\mathrm{core}}(x)\,\mathrm{d}x \tag{39a} \\ = {} & G_o^{\mathrm{L}}(x_{lp}) + c(x - x_{lp}) \\ & + p_1\big(G(x;0,\sigma_1) - G(x_{lp};0,\sigma_1)\big) \tag{39b} \\ = {} & p_1 G(x;0,\sigma_1) + c(x - x_{lp}) \\ & + (1-p_1) G(x_{lp};0,\sigma_2). \tag{39c} \end{aligned}$$

Let $G_o^{\mathrm{core}}(0) = G(0)$, the value of c is determined by

$$c = \frac{(1-p_1)\big(G(x_{lp};0,\sigma_2) - 0.5\big)}{x_{lp}}. \tag{40}$$

To prove that $G_o^{\mathrm{core}}(x)$ is the CDF overbound in the core region, we calculate the difference between $G_o^{\mathrm{core}}(x)$ and $G(x)$ as follows:

$$\begin{aligned} \Delta G(x) = {} & G_o^{\mathrm{core}}(x) - G(x) \\ = {} & \Big[p_1 G(x;0,\sigma_1) + c(x - x_{lp}) \\ & + (1-p_1) G(x_{lp};0,\sigma_2)\Big] \\ & - \Big[p_1 G(x;0,\sigma_1) \\ & + (1-p_1) G(x;0,\sigma_2)\Big] \\ = {} & c(x - x_{lp}) - (1-p_1) G(x;0,\sigma_2) \\ & + (1-p_1) G(x_{lp};0,\sigma_2). \end{aligned} \tag{41}$$

The first and second derivatives of $\Delta G(x)$ can be obtained by

$$\Delta G(x)' = c - (1-p_1) f_N(x;0,\sigma_2) \tag{42a}$$

$$\Delta G(x)'' = \frac{1-p_1}{\sigma_2^2 \sqrt{2\pi}} x \, \exp\left(-\frac{1}{2}\left(\frac{x}{\sigma_2}\right)^2\right). \tag{42b}$$

When $x_{lp} \le x < 0$, $\Delta G(x)''$ is negative over the domain, indicating that $\Delta G(x)$ is a concave function. We further examine the sign of $\Delta G(x)$ at the two endpoints as follows:

$$\Delta G(x_{lp}) = 0 \tag{43a}$$

$$\Delta G(0) = G_o^{\mathrm{core}}(0) - G(0) = 0. \tag{43b}$$

According to the definition of the concave function, for any $\omega \in [0, 1]$, the following equation holds:

$$\Delta G\big((1 - \omega)\, x_{lp} + \omega \times 0\big) \geq (1 - \omega)\, \Delta G\,(x_{lp}) + \omega \Delta G(0) = 0\,. \tag{44}$$

It is equivalent to saying that

$$\Delta G(x) \geq 0 \ \forall x_{lp} \leq \ x < 0\,. \tag{45}$$

Similarly, when $0 < x \leq x_{rp}$, $\Delta G(x)''$ is positive over the domain which means that, $\Delta G(x)$ is a convex function. The sign of $\Delta G(x)$ at x_{rp} is examined as follows:

$$\begin{aligned} \Delta G\,(x_{rp}) &= c\,(x_{rp} - x_{lp}) \\ &\quad - (1 - p_1)\, G\,(x_{rp}; 0, \sigma_2) \\ &\quad + (1 - p_1)\, G\,(x_{lp}; 0, \sigma_2)\,. \end{aligned} \tag{46}$$

By substituting (30), (40) and $G\,(x_{rp}; 0, \sigma_2) = 1 - G\,(x_{lp}; 0, \sigma_2)$ into (46), we can obtain that $\Delta G\,(x_{rp}) = 0$. According to the definition of the convex function, we have

$$\Delta G(x) \leq 0 \ \forall 0 \leq x \leq x_{lp}\,. \tag{47}$$

Combining (45) and (47), we can conclude that $G_o^{\text{core}}(x)$ is the CDF overbound of $G(x)$ at the core region.

The PGO of the BGMM with $p_1 = 0.9$, $\sigma_1 = 0.5$, and $\sigma_2 = 1.5$ is plotted in Fig. 2. In this example, the parameters of the PGO are computed as $k = 0.5881$ and $c = 0.0245$. In addition, the two-step Gaussian overbound [10] is also depicted for comparison. The plot reveals that the PDF and CDF of the PGO are closely aligned with those of BGMM in both the tail and core regions, compared to those of the two-step Gaussian overbound. The thumbnail in Fig. 2a illustrates the distribution of the PGO in the vicinity of the core-tail transition point, where the PDF of the PGO is not continuous at the transition point. Although the leap of PDF at the transition point is not negligible (calculated to be 0.06 through (31)), the CDF of the PGO appears exceptionally smooth near the core-tail transition point, as displayed in the thumbnail of Fig. 2b.

3. Sigma inflation

Equation (31) gives the overbound of the zero-mean BGMM distribution; however, in the application of bounding arbitrary sample distributions, samples may not be well characterized by the zero-mean BGMM distribution. In such a case, the PGO may not provide an overbound for these samples. These unbounded samples usually occur in the tails of the sample distribution. This is because samples in the central region usually exhibit a higher likelihood, and therefore the EM algorithm would prioritize the fitting performance of these central-region samples. In this section, we propose to inflate the tail of the PGO to tackle these unbounded samples.

The most straightforward approach is to increase σ_2. In the meanwhile, we have to ensure that the inflated PGO is the overbound of the before-inflation PGO and, thus, fitted zero-mean BGMM. Define σ_2^* as the inflated σ_2, and we have

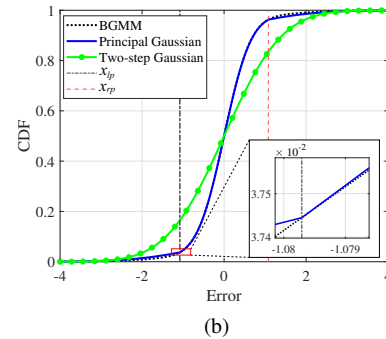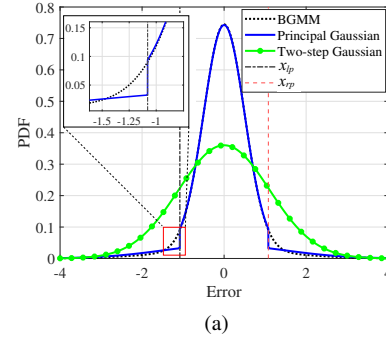$$\sigma_2^* = \tau_2 \sigma_2\,, \tag{48}$$

(a)

(b)

Fig. 2.   The (a) PDF and (b) CDF of the Principal Gaussian overbound of a zero-mean bimodal Gaussian mixture model with $p_1 = 0.9$, $\sigma_1 = 0.5$, and $\sigma_2 = 1.5$. The two-step Gaussian overbound is plotted for comparison.

where $\tau_2 > 1$ is the tail inflation factor. Then, the inflated tail bound can be written by

$$G_o^{\text{L}*}(x) = (1 + k^*)\,(1 - p_1)\, G\,(x; 0, \sigma_2^*) \ \ \forall x < x_{lp} \tag{49a}$$

$$k^* = \frac{p_1 G\,(x_{lp}; 0, \sigma_1)}{(1 - p_1)\, G\,(x_{lp}; 0, \sigma_2^*)}\,, \tag{49b}$$

where k^* is the new scaling parameter. Since $\sigma_2^* > \sigma_2$, we have $G\,(x_{lp}; 0, \sigma_2^*) > G\,(x_{lp}; 0, \sigma_2)$ and thus $k^* < k$. Therefore, it is difficult to compare the magnitude of $G_o^{\text{L}*}(x)$ and $G_o^{\text{L}}(x)$. A naive solution is to make $k^* = k$ by scaling σ_1 to σ_1^*, as shown below

$$\frac{p_1 G\,(x_{lp}; 0, \sigma_1^*)}{(1 - p_1)\, G\,(x_{lp}; 0, \sigma_2^*)} = \frac{p_1 G\,(x_{lp}; 0, \sigma_1)}{(1 - p_1)\, G\,(x_{lp}; 0, \sigma_2)}\,. \tag{50}$$

Indeed, (50) is satisfied only when σ_1^* is larger than σ_1.

We further check the bounding conditions in the core region by examining (39c) when $x < 0$. The first term $p_1 G(x; 0, \sigma_1)$ and the third term $(1 - p_1)G(x_{lp}; 0, \sigma_2)$ in (39c) will increase with the inflation in σ_1 and σ_2. The second term $c(x - x_{lp})$ in (39c) can be re-written by

$$c(x - x_{lp}) = \frac{(1 - p_1)\,\big(G(x_{lp}; 0, \sigma_2) - 0.5\big)(x - x_{lp})}{x_{lp}}\,, \tag{51}$$

where $x_{lp} \leq x < 0$ and $1 - p_1 > 0$. The inflation in σ_2 will increase the value of $G(x; 0, \sigma_2)$, thus enlarging $c(x - x_{lp})$. Therefore, $G_o^{\text{core}*}(x)$ with inflated σ_2 is larger than $G_o^{\text{core}}(x)$. In summary, the inflated PGO has the following property when $x < 0$,

$$\begin{cases} G_o^{\text{L}*}(x) > G_o^{\text{L}}(x) & \forall x < x_{lp} \\ G_o^{\text{core}*}(x) > G_o^{\text{core}}(x) & \forall x_{lp} \leq x < 0\,, \end{cases} \tag{52}$$

indicating that the inflated PGO is the overbound of the before-inflation PGO and, thus, the fitted BGMM.

In addition, unbounded samples may also occur in the core region, although such cases are rare. A slightly different inflation strategy could be applied. We only inflate the core of the PGO to bound these samples. Define σ_1^* as the inflated σ_1, and we have

$$\sigma_1^* = \tau_1 \sigma_1 \,, \tag{53}$$

where $\tau_1 > 1$ is the core inflation factor. The inflation of σ_1 only affects the value of $G(x; 0, \sigma_1)$ in $G_o^{\text{core}}(x)$ and k in $G_o^{\text{L}}(x)$. Actually, both $G(x; 0, \sigma_1)$ and k are increased by inflating σ_1, thereby enlarging the value of $G_o^{\text{core}}(x)$ and $G_o^{\text{L}}(x)$ when $x < 0$. As a result, the same conclusion as in (52) can be drawn. Our inflation strategies in both tail and core regions can ensure the preservation of overbounding properties with respect to the fitted BGMM.

The inflation of σ_2 and σ_1 can be realized by an iterative approach. In each iteration, we inflate σ_2 or σ_1 according to the violation of bounding conditions with a small and fixed inflation factor. Based on the inflated PGO, all samples are examined for the violation of bounding conditions. The iteration process will stop once all samples are CDF overbounded by the inflated PGO. The pseudocode of the sigma inflation strategy is given in Appendix F. In addition, Appendix G shows summarize the steps for implementing PGO.

D. Preservation of Overbounding Property

In this section, we use DeCleene's theorem [9] to prove that the overbounding property of the PGO can be preserved through convolution; more specifically, to prove that the overbounding property can be preserved between the range and position domain. Given that $G_{oa}(x)$ and $G_{ov}(x)$ are the overbound distribution of the error distribution $G_a(x)$ and $G_v(x)$, respectively, it is essential for the overbound distribution to have the following property:

$$G_{oa+ov}(x) \text{ overbound } G_{a+v}(x) \,. \tag{54}$$

DeCleene proves that the above property is established if $G_{oa}(x)$, $G_{ov}(x)$, $G_a(x)$, and $G_v(x)$ are all unimodal and symmetric distributions [9].

In this paper, the zero-mean BGMM in (18) and the PGO in (31) are inherently symmetric distributions. Therefore, we only need to prove the unimodality of these distributions. The first derivative of the PDF of the zero-mean BGMM is given by

$$
\begin{aligned}
f'(x) = & -\frac{x}{\sigma_1^2} \cdot p_1 f_N(x; 0, \sigma_1) \\
& -\frac{x}{\sigma_2^2} \cdot (1 - p_1) f_N(x; 0, \sigma_2) \,.
\end{aligned} \tag{55}
$$

Clearly,

$$f'(x) > 0 \ \forall x < 0, \ f'(0) = 0, f'(x) < 0 \ \forall x > 0. \tag{56}$$

Therefore, the zero-mean BGMM is a unimodal distribution.

For the PGO, Appendix C proves that $f_o(x)$ is a monotonically increasing function when $x < 0$. According to the symmetric property of $f_o(x)$, we can conclude that $f_o(x)$ is a monotonically decreasing function when $x \geq 0$. Therefore, $f_o(x)$ is a unimodal function. This ends the proof that the overbounding property of the PGO is preserved through convolution.

E. Position-Domain Bounding

1. Overbound of positioning error

In GNSS positioning, it is essential to project the range-domain error to the position-domain error as it allows us to estimate the accuracy of the positioning results obtained from GNSS measurements. For single point positioning or DGNSS positioning, a general relationship between range-domain error and position-domain error is determined by [26], [27]

$$\Delta \mathbf{x} = \mathbf{S} \Delta \rho \,, \tag{57}$$

where $\Delta \mathbf{x}$ is the estimation error vector, including the three-dimensional position error and the clock error (exists in the single point positioning), $\Delta \rho = [\rho_1, \rho_2, \ldots, \rho_N]$ is the measurement error vector in the range-domain, N is the number of measurements, and $\mathbf{S}$ is the solution matrix obtained from the least square solution. Although the forms of $\Delta \mathbf{x}$, $\Delta \rho$, and $\mathbf{S}$ are different for the two positioning methods, a common logic is shared. Assuming that the third element of $\Delta \mathbf{x}$ is the vertical position error (VPE), the third row of (57) can be extracted and written as

$$\text{VPE} = \sum_{i=1}^N s_{3,i} \Delta \rho_i \,, \tag{58}$$

where $s_{3,i}$ refers to the ith element of the third row in the $\mathbf{S}$ matrix. Let

$$Y_i^{r_i} = s_{3,i} \Delta \rho_i, \ i = 1, 2, \cdots, N \tag{59}$$

be a new random variable, and then VPE can be written by

$$\text{VPE} = \sum_{i=1}^N Y_i^{r_i} \,. \tag{60}$$

The PDF of VPE can be obtained through convolution as

$$f_{\text{VPE}}(x) = f_{Y_1}^{r_1}(x) * f_{Y_2}^{r_2}(x) * \ldots * f_{Y_N}^{r_N}(x) \,, \tag{61}$$

where

$$f_{Y_i}^{r_i}(x) = \frac{1}{|s_{3,i}|} f_{r_i}\left(\frac{x}{|s_{3,i}|}\right) \tag{62}$$

is the PDF of $Y_i^{r_i}$, $f_{r_i}(x)$, $i = 1, 2, \cdots, N$ is the PDF of the ith measurement error, and $*$ is the convolution operation. A proof of (62) is provided in Appendix D. Assuming the distribution of $f_{r_k}(x)$ has the largest variance σ_k^2, the most conservative VPE distribution is given by

$$f_{\text{VPE}}(x) = f_{Y_1}^{r_k}(x) * f_{Y_2}^{r_k}(x) * \ldots * f_{Y_N}^{r_k}(x) \,. \tag{63}$$

Then, the VPE can be bounded by

$$f_{o,\text{VPE}}(x) = f_{o,Y_1}(x) * f_{o,Y_2}(x) * \ldots * f_{o,Y_N}(x) \,, \tag{64}$$

where

$$f_{o,Y_i}(x) = \frac{1}{|s_{3,i}|} f_o\left(\frac{x}{|s_{3,i}|}\right), \qquad (65)$$

and $f_o(x)$ is the PGO of $f_{r_k}(x)$.

2. Fourier transform

The convolution operation in (64) involves the PGO, which is defined as a piecewise function in (31). This can be a challenging task due to the complexity of the function. However, the Fourier transform (FT) [28], denoted as $\mathcal{F}(\cdot)$, provides an alternative way to compute the distribution of $f_{o,\text{VPE}}(x)$. According to the convolution theorem, the Fourier transform of $f_{o,\text{VPE}}(x)$ can be expressed by

$$\begin{aligned}
\mathcal{F}(f_{o,\text{VPE}}(x)) &= \mathcal{F}(f_{o,Y_1}(x)) \cdot \mathcal{F}(f_{o,Y_2}(x)) \\
&\quad \cdot \ldots \cdot \mathcal{F}(f_{o,Y_N}(x)),
\end{aligned} \qquad (66)$$

where $\cdot$ denotes the point-wise multiplication. The distribution of $f_{o,\text{VPE}}(x)$ is recovered by the inverse Fourier transform (IFT) as follows:

$$\begin{aligned}
f_{o,\text{VPE}}(x) = \mathcal{F}^{-1}\Big(&\mathcal{F}(f_{o,Y_1}(x)) \\
&\cdot \mathcal{F}(f_{o,Y_2}(x)) \cdot \ldots \cdot \mathcal{F}(f_{o,Y_N}(x)) \Big).
\end{aligned} \qquad (67)$$

In practice, the FT and IFT are realized by discrete Fourier transform (DFT) and its inverse (IDFT) [28], respectively, which means the PDF $f_{o,Y_i}(x)$ should be discretized. According to DeCleene's theorem [9], the discrete model should be the overbound for the continuous distribution it replaces. However, the discretization strategy that directly samples the PDF at equal intervals cannot guarantee the preservation of overbounding properties. Therefore, we propose an alternative discretization strategy, as illustrated in the next section.

3. Discretization satisfying overbounding

Inspired by the discrete overbounding model proposed in [29], we propose to discretize the CDF related to $f_{o,Y_i}(x)$, which can be formalized as follows:

$$\begin{aligned}
F_{o,Y_i}(x) &= \int_{-\infty}^{x} f_{o,Y_i}(x)\,dx = \int_{-\infty}^{x} \frac{1}{|s_{3,i}|} f_o\left(\frac{x}{|s_{3,i}|}\right) dx \\
&= F_o\left(\frac{x}{|s_{3,i}|}\right),
\end{aligned} \qquad (68)$$

where $F_o(x)$ is the CDF of the PGO for $f_{r_k}(x)$. The discretization process can be regarded as constructing a discretized overbound distribution for $F_{o,Y_i}(x)$. Specifically, Let $2L-1$ be the length of the discretized sequence, and T be the sampling interval (unit: meter), and then we can (almost) equally divide the domain of $F_{o,Y_i}(x)$ into $2L$ intervals, including $(-\infty, x_1), [x_1, x_2), ..., [x_{2L-2}, x_{2L-1})$, and $[x_{2L-1}, \infty)$, where $x_n = (n - L)T$, $n = 1, 2, \cdots, 2L-1$. The discretization results are shown in Fig. 3a, where each interval has equal length T except the first and the last interval. The discrete CDF overbound of $F_{o,Y_i}(x)$ is

formalized as a piecewise function as follows:

$$\begin{aligned}
&F_{D,Y_i}(x) \\
&= \begin{cases}
F_{o,Y_i}(x) & \text{if } x < x_1 \\
F_{o,Y_i}(x_{n+1}) & \text{if } x_n \le x < x_{n+1}, 1 \le n < L-1 \\
F_{o,Y_n}(x_n) & \text{if } x_n \le x < x_{n+1}, L-1 \le n < 2L-2 \\
F_{o,Y_i}(x) & \text{if } x \ge x_{2L-1}
\end{cases}.
\end{aligned} \qquad (69)$$

As can be seen, the discrete model $F_{D,Y_i}(x)$ is the overbound for the continuous model $F_{o,Y_i}(x)$. The probability mass function (PMF) of $F_{D,Y_i}(x)$ can be calculated by

$$\begin{aligned}
&p_{D,Y_i}(x) \\
&= \begin{cases}
F_{D,Y_i}(x_1) - F_{o,Y_i}(x_1) & \text{if } x = x_1 \\
F_{D,Y_i}(x_n) - F_{D,Y_i}(x_{n-1}) & \text{if } x = x_n, 1 < n \le 2L-1 \\
0 & \text{otherwise}
\end{cases},
\end{aligned} \qquad (70)$$

which has a discrete nature. The discretization process is completed by evaluating $p_{D,Y_i}(x)$ at the $2L-1$ points as follows:

$$Y_{o,i}[n] = p_{D,Y_i}(x_n), \ n = 1, 2, \cdots, 2L-1. \qquad (71)$$

Then, the PMF of the VPE overbound in the discretized form can be obtained by the discrete convolution as follows:

$$Y_{o,\text{VPE}}[n] = (Y_{o,1} * Y_{o,2} * \ldots * Y_{o,N})[n]. \qquad (72)$$

By taking the discrete convolution theorem, $Y_{o,\text{VPE}}[n]$ can be computed as

$$\begin{aligned}
Y_{o,\text{VPE}}[n] &= \mathcal{F}_D^{-1}\Big(\mathcal{F}_D(Y_{o,1}) \cdot \mathcal{F}_D(Y_{o,2}) \cdot \ldots \\
&\quad \cdot \mathcal{F}_D(Y_{o,N})\Big), \ n = 1, 2, \cdots, L_o \\
L_o &= N \times (2L-2) + 1,
\end{aligned} \qquad (73)$$

where $\mathcal{F}_D(\cdot)$ and $\mathcal{F}_D^{-1}(\cdot)$ denote the DFT and IDFT [28], respectively. Note that the length of $Y_{o,\text{VPE}}[n]$ is extended to $N \times (2L-2) + 1$. This is because the length of the resulting sequence in the convolution is given by $L_1 + L_2 - 1$, where L_1 and L_2 are the lengths of two input sequences, respectively. In addition, the convolution process does not change the sampling interval; therefore, the distance of the domain of any two adjacent elements in $Y_{o,\text{VPE}}[n]$ is T, which is the same as that in $Y_{o,i}[n]$. The DFT is usually implemented by the fast Fourier transform algorithm [17] in the modern software solution or even dedicated hardware, whose computational complexity is only $O((L_e)\log(L_e))$, where L_e is the length of the input sequence and $L_e = 2L-1$ in our case.

4. Calculation of protection level

The discrete sequence $Y_{o,\text{VPE}}[n]$ in (73) can be interpreted as the PMF of the VPE overbound evaluated at $t_n = (n - \frac{L_o+1}{2})T$. Here we use a different notation t to represent the domain of $Y_{o,\text{VPE}}[n]$ without loss of generality. The VPL can be obtained by finding the index
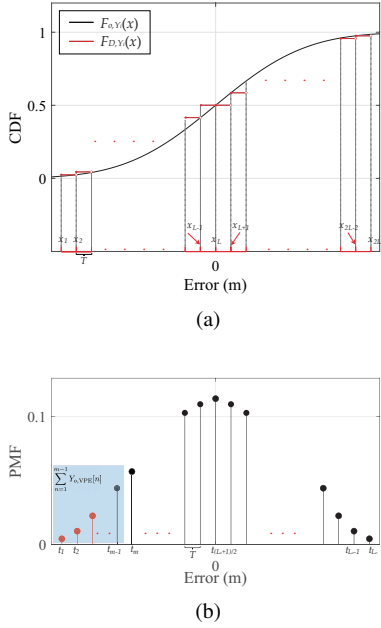
(a)

(b)

Fig. 3. Demonstrations of (a) the discretization process and (b) the PL searching process. The shaded area in (b) shows the cumulative probability from t_1 to t_{m-1}.

$m \in \{1, \ldots, L_o\}$ that satisfies the following conditions:

$$\sum_{n=1}^{m-1} Y_{o,\mathrm{VPE}}[n] < \frac{1}{2} P_{\mathrm{HMI}}$$
$$\sum_{n=1}^{m} Y_{o,\mathrm{VPE}}[n] \geq \frac{1}{2} P_{\mathrm{HMI}} , \tag{74}$$

where $\sum_{n=1}^{m-1} Y_{o,\mathrm{VPE}}[n]$ is the cumulative probability from t_1 to t_{m-1}, as shown in Fig. 3b, and P_{HMI} is the specified probability of hazardously misleading information. The VPL is given by

$$\mathrm{VPL} = |t_{m-1}| = \left| \left((m-1) - \frac{L_o+1}{2} \right) T \right|. \tag{75}$$

V. BOUNDING PERFORMANCE ANALYSIS

This section analyzes the bounding performance of the proposed PGO on the DGNSS pseudorange data. We compare the proposed method with the following two methods:

1) Two-step Gaussian overbound: a typical paired overbounding method that utilizes two Gaussian distributions to overbound the left-side and right-side error distribution separately [10]. For practical applications, the bias terms in the left side and the right side overbounds are set to be the same;
2) Gaussian-Pareto overbound: a recently developed core overbounding method that bounds the core part of the error with Gaussian distribution and bounds the tail part with the generalized Pareto distribution [4].

Two datasets, including the DGNSS pseudorange data collected from two Continuously Operating Reference Stations in Minneapolis (Section V.B) and the DGNSS pseudorange data collected from a slightly urbanized area in Hong Kong (Section V.C), are employed for bounding performance comparison. All computations are conducted on a laptop (Intel Core i7-12700H CPU, 2.30 GHz). A brief introduction to DGNSS error and positioning is given in Section V.A.

A. DGNSS Error and Positioning

1. DGNSS error calculation

The double-differenced pseudorange model [30] is given by

$$\nabla \Delta \rho_{r_1,r_2}^{s,i} = \nabla \rho_{r_1,r_2}^{s} - \nabla \rho_{r_1,r_2}^{i}$$
$$= \left(r_{r_1}^{s} - r_{r_2}^{s} \right) - \left(r_{r_1}^{i} - r_{r_2}^{i} \right) + \varepsilon_{r_1,r_2}^{s,i} , \tag{76}$$

where $\nabla \rho_{r_1,r_2}^{s}$ is the difference between the pseudorange measurements of receivers r_1 and r_2 regarding the satellite s, $\nabla \rho_{r_1,r_2}^{i}$ is the difference between the pseudorange measurements of receivers r_1 and r_2 regarding the satellite i; $r_{r_1}^{s}$, $r_{r_2}^{s}$, $r_{r_1}^{i}$, and $r_{r_2}^{i}$ are the actual distance between r_1 and s, r_2 and s, r_1 and i, and r_2 and i, respectively; and $\varepsilon_{r_1,r_2}^{s,i}$ is the DGNSS error. In this work, we assume s is the master satellite without any loss of generality. With the double differencing, common errors, including the receiver clock bias, satellite clock bias, ionospheric delay, and tropospheric delay, are eliminated. The detailed derivation of the double-differenced pseudorange model can refer to Larson's work [4].

Let $\mathbf{x}^s$ be the position of satellite s, $\mathbf{x}^i$ be the position of satellite i, $\mathbf{x}_{r_1}$ be the position of receiver r_1, and $\mathbf{x}_{r_2}$ be the position of the receiver r_2. $\mathbf{x}^s$, $\mathbf{x}^i$, $\mathbf{x}_{r_1}$, and $\mathbf{x}_{r_2}$ are all defined in the Earth-Centered, Earth-Fixed (ECEF) frame. Then (76) can be written as

$$\nabla \Delta \rho_{r_1,r_2}^{s,i} = \left(\|\mathbf{x}^s - \mathbf{x}_{r_1}\| - \|\mathbf{x}^s - \mathbf{x}_{r_2}\| \right)$$
$$- \left(\|\mathbf{x}^i - \mathbf{x}_{r_1}\| - \|\mathbf{x}^i - \mathbf{x}_{r_2}\| \right) \tag{77}$$
$$+ \varepsilon_{r_1,r_2}^{s,i} .$$

The DGNSS errors $\varepsilon_{r_1,r_2}^{s,i}$ can be characterized with the information of $\nabla \Delta \rho_{r_1,r_2}^{s,i}$, $\mathbf{x}^s$, $\mathbf{x}^i$, $\mathbf{x}_{r_1}$, and $\mathbf{x}_{r_2}$.

2. DGNSS positioning

In this section, we assume that $\mathbf{x}_{r_2}$ is known and $\mathbf{x}_{r_1} = [x, y, z]^T$ is the position to be estimated in the DGNSS positioning. Let $\hat{\mathbf{x}}_{r_1} = [\hat{x}_{r_1}, \hat{y}_{r_1}, \hat{z}]^T$ be the current guess of $\mathbf{x}_{r_1}$, and then the current guess of $\nabla \Delta \rho_{r_1,r_2}^{s,i}$ is given by

$$\nabla \Delta \hat{\rho}_{r_1,r_2}^{s,i} = \left(\|\mathbf{x}^s - \hat{\mathbf{x}}_{r_1}\| - \|\mathbf{x}^s - \mathbf{x}_{r_2}\| \right)$$
$$- \left(\|\mathbf{x}^i - \hat{\mathbf{x}}_{r_1}\| - \|\mathbf{x}^i - \mathbf{x}_{r_2}\| \right) . \tag{78}$$

Equation (77) can be approximated with the Taylor series with respect to $\hat{\mathbf{x}}_{r_1}$ by

$$\nabla \Delta \rho_{r_1,r_2}^{s,i} = \nabla \Delta \hat{\rho}_{r_1,r_2}^{s,i} + \left(e_{r_1,x}^{s} - e_{r_1,x}^{i} \right) \sigma x$$
$$+ \left(e_{r_1,y}^{s} - e_{r_1,y}^{i} \right) \sigma y$$
$$+ \left(e_{r_1,z}^{s} - e_{r_1,z}^{i} \right) \sigma z \tag{79a}$$

$$\mathbf{e}_{r_1}^s = \begin{bmatrix} e_{r_1,x}^s & e_{r_1,y}^s & e_{r_1,y}^s \end{bmatrix}^T$$

$$= \begin{bmatrix} \dfrac{\hat{x}_{r_1}-p_x^s}{\|\mathbf{x}^s-\hat{\mathbf{x}}_{r_1}\|} & \dfrac{\hat{y}_{r_1}-p_y^s}{\|\mathbf{x}^s-\hat{\mathbf{x}}_{r_1}\|} & \dfrac{\hat{z}_{r_1}-p_z^s}{\|\mathbf{x}^s-\hat{\mathbf{x}}_{r_1}\|} \end{bmatrix}^T \tag{79b}$$

$$\Delta\mathbf{x} = \begin{bmatrix} \sigma x & \sigma y & \sigma z \end{bmatrix}^T, \tag{79c}$$

where $\mathbf{e}_{r_1}^s$ is known as the line-of-sight (LOS) vector between the satellite s to the receiver r_1, and $\Delta\mathbf{x} = \mathbf{x}_{r_1} - \hat{\mathbf{x}}_{r_1}$ is the positioning error. The least square (LS) method is employed to estimate the positions of r_1. Assuming that satellite s is chosen as the master satellite and N DGNSS measurements are obtained at the current epoch, the positioning system can be formulated as the following LS problem:

$$\Delta\mathbf{x} = \underset{\Delta\mathbf{x}}{\arg\min} \|\Delta\rho_d - \mathbf{H}\Delta\mathbf{x}\|. \tag{80}$$

where

$$\Delta\rho_d = \begin{bmatrix} \nabla\Delta\rho_{r_1,r_2}^{s,1} - \nabla\Delta\hat{\rho}_{r_1,r_2}^{s,1} \\ \vdots \\ \nabla\Delta\rho_{r_1,r_2}^{s,N} - \nabla\Delta\hat{\rho}_{r_1,r_2}^{s,N} \end{bmatrix} \tag{81a}$$

$$\mathbf{H} = \begin{bmatrix} \left(\mathbf{e}_{r1}^s - \mathbf{e}_{r1}^1\right)^T \\ \vdots \\ \left(\mathbf{e}_{r1}^s - \mathbf{e}_{r1}^N\right)^T \end{bmatrix}. \tag{81b}$$

The solution of this LS problem is

$$\Delta\mathbf{x} = \left(\mathbf{H}^T\mathbf{H}\right)^{-1}\mathbf{H}^T\Delta\rho_d, \tag{82}$$

where $\left(\mathbf{H}^T\mathbf{H}\right)^{-1}\mathbf{H}^T$ is the solution matrix, as illustrated in (57) in Section IV.E.

B. CORS DGNSS Error Bounding

1. CORS DGNSS dataset

Inspired by work in [4], this paper utilizes reference station data from the CORS website run by the National Geodetic Survey (NGS), specifically from stations MNAV and ZMP1. These stations are situated near Minneapolis, with an approximate distance of $11.5\,\mathrm{km}$ between them. The position of the two reference stations is calculated by Precise Point Positioning [30]. The satellite position in the ECEF frame is calculated based on the broadcast ephemeris from NASA's Archive of Space Geodesy Data website [31] by utilizing RTKLIB [32]. For each double-differenced pseudorange in (77), the master satellite is selected as the satellite with the highest elevation angle at that time epoch. Our research encompasses data from January 1st, 2020 to December 31st, 2020. As GPS data is strongly influenced by the elevation angle, the collected samples are organized into bins based on elevation angles every $5°$ from $15°$ to $80°$, which encompasses the highest elevation angle observed in the data.

2. Comparison of DGNSS error bounding

Fig. 4a shows the quantile-quantile (QQ) plot of DGNSS errors for elevation angles observed from $30°$ to $35°$ over one month. The QQ plot shows the quantile of error distribution with the equivalent standard normal quantile, such that the Gaussian distributed error exhibits a straight line. As can be seen, the DGNSS error has heavy tails, which is potentially due to multipath effects. The CDFs of the two-step Gaussian overbound, Gaussian-Pareto overbound, and the proposed PGO are plotted in Fig. 4b. The fitted BGMM of the DGNSS error is also plotted in Fig. 4b for comparison. Note that the two-step Gaussian overbound has two parts, i.e., two-step Gaussian (L) and two-step Gaussian (R), which represent the overbound at the left region ($x < 0$) and the right region ($x \geq 0$), respectively. It is shown that the proposed PGO exhibits a tighter CDF overbound than the two-step Gaussian overbound in the core region of the error distribution.

To further analyze the bounding performance at the tail region, we plot the CDF and complementary cumulative distribution function (CCDF) of each overbounding method on a logarithmic scale. The logarithmic CDF in Fig. 4c shows the bounding results at the left tail region, and the logarithmic CCDF in Fig. 4d demonstrates the results at the right tail region. It is impressive that the Gaussian-Pareto overbound shows the sharpest bound at both the left and right tail regions. This is because the Gaussian-Pareto overbounding method divides the samples into two individual parts (core and tail parts) and bounds each part separately. In the tail part bounding, the Gaussian-Pareto overbounding method uses the generalized Pareto distribution, which is especially suitable for modeling extreme tails that extend beyond the range of available data [4]. The PGO shows moderate bounding performance at the tail region, which has a tighter bound than the two-step Gaussian overbound but not as tight as the Gaussian-Pareto overbound. However, the PGO has its own advantages in that its overbounding property can be preserved through convolution, which is essential in the range-to-position projection process and the calculation of PLs. It is worth noting that the fitted BGMM fails to overbound the sample distribution, as shown in the region of $x \in [4\,\mathrm{m}, 5\,\mathrm{m}]$ in Fig. 4d. This is because the fitted BGMM can only fit the overall pattern of the sample distribution and is not guaranteed to bound the sample distribution. The parameters of the Principal Gaussian, two-step Gaussian, and Gaussian-Pareto overbounding methods are listed in Appendix H.

Fig. 5 shows the bounding results of DGNSS errors for elevation angles observed from $30°$ to $35°$ over the course of one year. The extension of the data collection period increases the chances of observing more extreme data. The maximum absolute DGNSS error reaches $8.64\,\mathrm{m}$, which is around 21% larger than that observed in the one-month DGNSS error data ($7.12\,\mathrm{m}$ in this case). Nevertheless, the PGO still yields a considerably tight bound in the core region and shows moderate overall bounding performance among the three overbounding methods.

Fig. 6 shows the bounding results of DGNSS errors for the elevation angle bin of $60°$ to $65°$ over one year. In this case, the sample distribution is not significantly
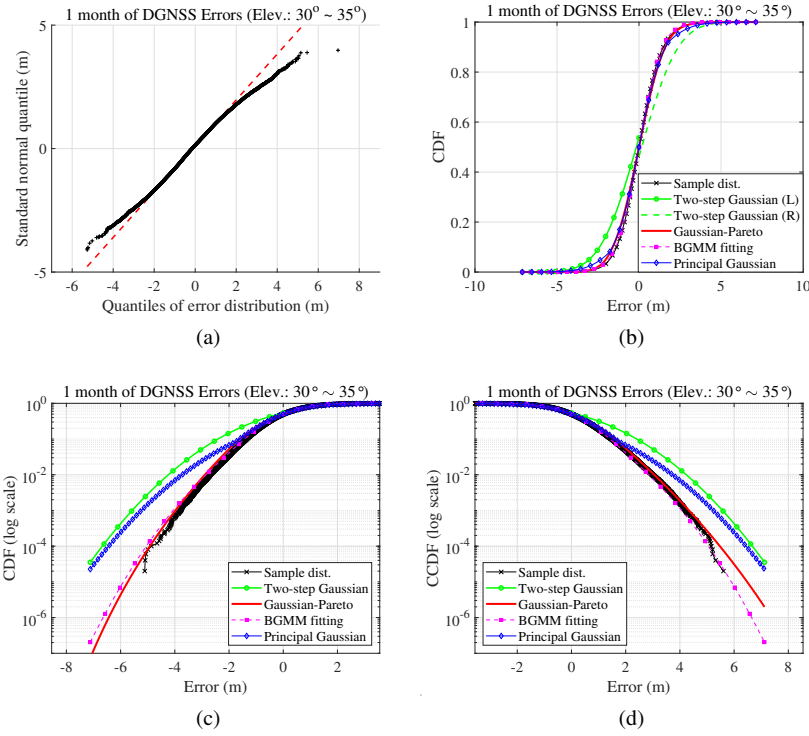
Fig. 4.   (a) The QQ plot of CORS DGNSS errors for elevation angles observed from $30°$ to $35°$ over one month; and the distribution of three overbounding methods in three views: (b) CDF; (c) CDF plotted on a logarithmic scale; (d) complementary cumulative distribution function (CCDF) plotted on a logarithmic scale, where "Two-step Gaussian (L)" and "Two-step Gaussian (R)" represent the two-step Gaussian overbound at the left region and the right region, respectively.
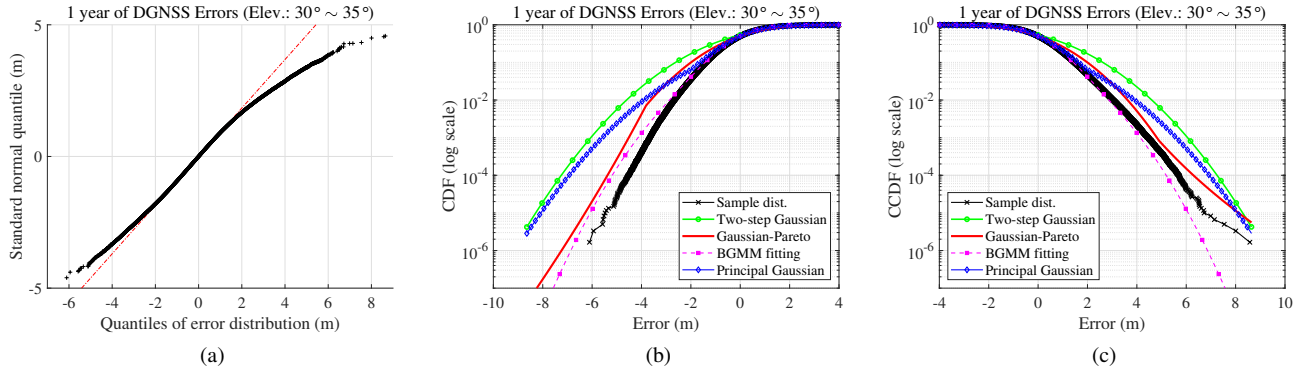

Fig. 5.   (a) The QQ plot of CORS DGNSS errors for elevation angles observed from $30°$ to $35°$ over one year; and the distribution of three overbounding methods in two views: (b) CDF plotted on a logarithmic scale; (c) CCDF plotted on a logarithmic scale, where "Two-step Gaussian (L)" and "Two-step Gaussian (R)" represent the two-step Gaussian overbound at the left region and the right region, respectively.

heavy-tailed, as suggested by the QQ plot in Fig. 6a. One potential explanation is that the underlying error sources contributing to the heavy tail in the GNSS error distribution, such as multi-path or significant atmospheric disturbances, are absent at high elevation angles. This phenomenon is also observed in Larson's work on DGNSS error bounding [4]. In such a situation, there seems to be no significant difference among the three overbounding methods, as shown in Fig. 6b and Fig. 6c. Therefore, it is recommended to use the Gaussian overbound when the sample distribution does not exhibit heavy-tailed properties, as the Gaussian overbound has

fewer parameters to determine. The bounding results of one-year DGNSS error in every $5°$ from $15°$ to $80°$ can refer to Appendix K (a masking angle of $15°$ is applied), where similar conclusions are drawn.

C. Urban DGNSS Error Bounding

1. Urban DGNSS dataset

To comprehensively validate the proposed method, we conducted an additional experiment on an urban dataset, which is collected from a slightly urbanized area in Hong Kong, as shown in Fig. 7. The term "slightly urbanized"
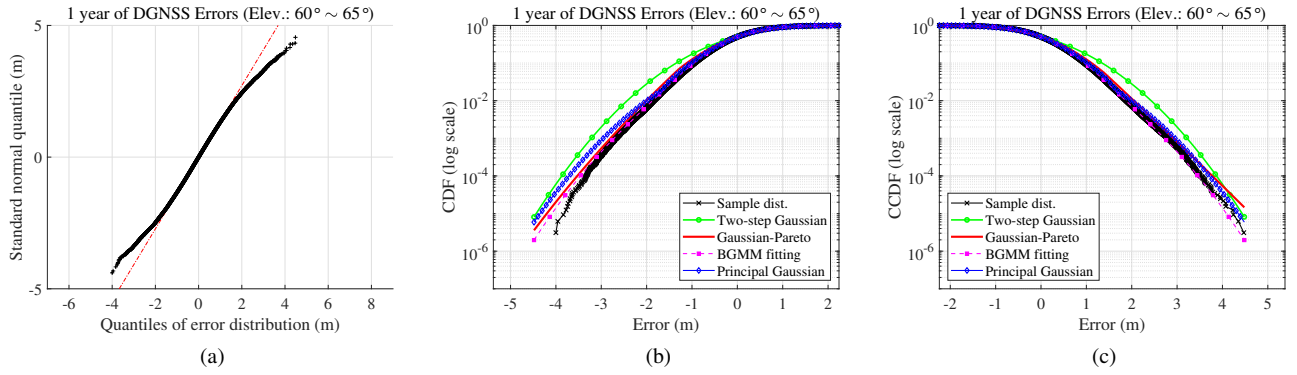
Fig. 6. (a) The QQ plot of CORS DGNSS errors for elevation angles observed from $60°$ to $65°$ over one year; and the distribution of three overbounding methods in two views: (b) CDF plotted on a logarithmic scale; (c) CCDF plotted on a logarithmic scale, where "Two-step Gaussian (L)" and "Two-step Gaussian (R)" represent the two-step Gaussian overbound at the left region and the right region, respectively.

indicates that the vicinity of the receiver's position is not dominated by high-rise buildings. As can be seen, the receiver is located along the sea, and buildings in nearshore areas may block or reflect satellite signals, resulting in a multipath effect. Fig. 7 also shows the setup of the experimental platform. The U-blox Zed F9P is employed to collect L1 GPS, BeiDou, and GLONASS signals at a frequency of 1 Hz, producing a dataset with a duration of 57 minutes. The receiver's location is determined by real-time kinematic (RTK) positioning [32]. The filter type is the combined mode, the integer ambiguity resolution is fix and hold mode, and the ratio to fix ambiguity is set to be 5. The final fix rate is 95.5%. The satellite position in the ECEF frame is calculated based on the broadcast ephemeris from Hong Kong Geodetic Survey Services [33] by utilizing RTKLIB [32].
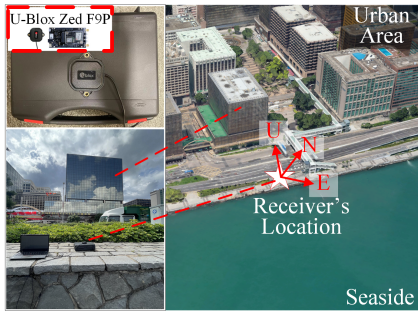

Fig. 7. The experimental environment and platform for collecting urban DGNSS data.

Fig. 8 plots the absolute DGNSS errors against the elevation angle and signal-to-noise ratio (SNR) related to the receiver. In this experiment, the DGNSS measurements with the elevation angle larger than $30°$ and SNR greater than $35\,\text{dB}$ are selected for DGNSS positioning. Within this interval, the DGNSS measurement appears to be free of faults since its error is limited in a reasonable range where the maximum absolute error is around $13.25\,\text{m}$. Appendix I shows the histogram of DGNSS error with SNR greater than $35\,\text{dB}$ and elevation angles larger than $30°$ in each $5°$ elevation angle bin. We select the DGNSS

error for elevation angles observed from $30°$ to $35°$ for analysis in the following sections, whose mean value is nearly zero. The DGNSS errors in bins $35° \sim 40°$ and $50° \sim 55°$ also have nearly zero mean values. Their bounding results are presented in Appendix J due to the space limit.
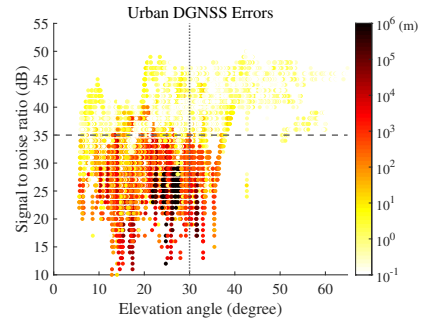

Fig. 8. The absolute DGNSS errors in the urban dataset against the elevation angle and signal-to-noise ratio related to the receiver. The color bar represents the magnitude of the absolute DGNSS errors and is plotted on a logarithmic scale.

2. Comparison of DGNSS error bounding

Fig. 9a shows the QQ plot of urban DNGSS error for elevation angles observed from $30°$ to $35°$, where a significant heavy-tailed phenomenon is observed. In this case, the proposed PGO shows the sharpest bounding performance in the core region among all the three methods, as shown in Fig. 9b. In the tail region, the PGO has a tighter bound than the two-step Gaussian overbound, as shown in Fig. 9c and Fig. 9d. The Gaussian-Pareto overbound shows the best bounding performance in the tail and core regions, but it also shows extreme asymmetry in the left and right side tail regions. This asymmetry is actually attributed to the asymmetry of the sample distribution whose left tail is much heavier than the right tail, as shown in Fig. 9c and Fig. 9d. The Gaussian-Pareto overbounding method bounds the left and right tails separately, thereby resulting in different bounding results on the two sides. This asymmetry causes difficulties in preserving the overbounding properties after
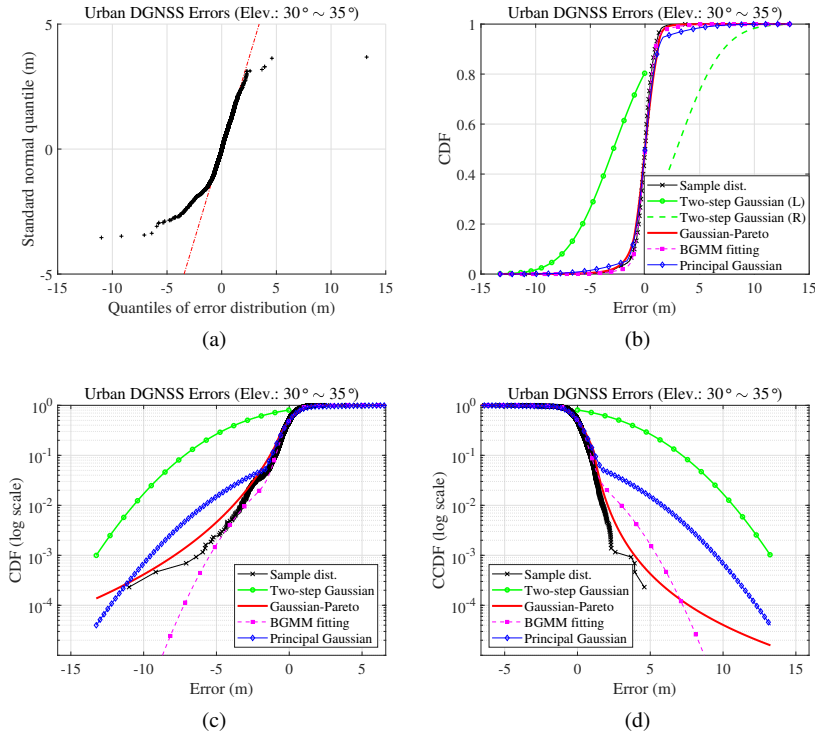
Fig. 9.   (a) The QQ plot of urban DGNSS errors for elevation angles observed from $30°$ to $35°$; and the distribution of three overbounding methods in three views: (b) CDF; (c) CDF plotted on a logarithmic scale; (d) CCDF plotted on a logarithmic scale, where "Two-step Gaussian (L)" and "Two-step Gaussian (R)" represent the two-step Gaussian overbound at the left region and the right region, respectively.

convolution, making it impossible to calculate the PL. This, on the other hand, highlights the benefits of applying the proposed method to bound the extremely heavy-tailed distribution, as it enables the computation of PL for integrity-assured applications.

3. Comparison of position error bounding

Fig. 10a shows a time series of VPE produced by the DGNSS positioning method (Section V.A). The mean VPE is $0.65\,\mathrm{m}$ and the maximum VPE is $6.44\,\mathrm{m}$. The VPL (with $P_{\mathrm{HMI}} = 10^{-9}$) of the positioning results from the two overbounding methods, including the PGO and the two-step Gaussian overbound, is also plotted in the figure. The VPL is calculated based on the worst-case DGNSS error distribution, i.e., the error distribution shows the largest variance. In this experiment, the worst-case DGNSS error distribution is given by the error for elevation angles observed from $30°$ to $35°$. In the PGO approach, the discretization parameters in the VPL calculation are set as $T = 0.01\,\mathrm{m}$ and $2L-1 = 6001$, as defined in Section IV.E. A discussion about the choice of T is given in Appendix E. The Gaussian-Pareto overbound is not taken for comparison since its overbounding property cannot be preserved through convolution.

As shown in Fig. 10a, the PGO yields a significantly smaller VPL than the two-step Gaussian overbound at every epoch. Table I lists the reduction of VPL by the PGO. The mean VPL is reduced by more than $78\,\%$ while the maximum reduction even reaches $80\,\%$. The triangular charts in Fig. 10c and Fig. 10d show that

integrity is preserved for both overbounding methods. However, the VPL yielded by the PGO is smaller and exhibits a higher concentration level than that of the two-step Gaussian overbound. These plots indicate that the PGO can significantly reduce PLs without compromising integrity.

TABLE I
The reduction of VPL by the Principal Gaussian overbound compared to the two-step Gaussian overbound

Min	Max	Mean	Median
$72.27\,\%$	$80.48\,\%$	$78.61\,\%$	$78.79\,\%$

Fig. 10b plots the computation time of VPL with the PGO against the number of DGNSS measurements through the Monte Carlo simulation. For fifteen measurements, the mean computation time is only $0.08\,\mathrm{s}$, which is well acceptable for a personal computer. The small computation load is achieved by using the fast Fourier transform to calculate the overbound distribution in the position domain instead of using direct convolution operations, as shown in (73).

VI. DISCUSSION

A. Impacts of the Partition Parameter

In this section, we discuss the impacts of parameter setting on the performance of the PGO. Here, the PGO refers to the one without sigma inflation. This is because
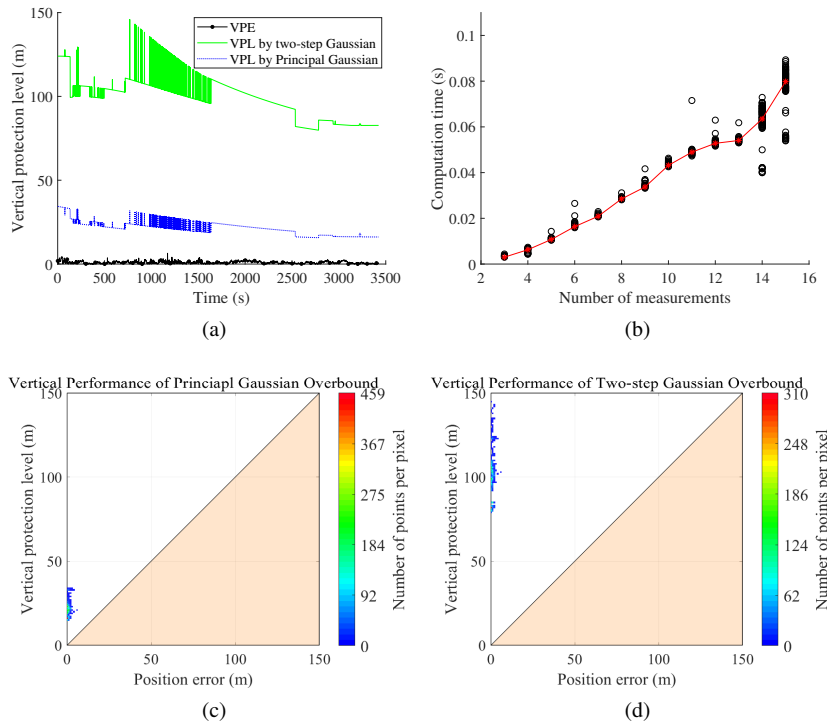
Fig. 10. (a) The time series of VPE and VPL with $P_{\mathrm{HMI}} = 10^{-9}$; (b) The computation time of VPL with the Principal Gaussian overbound against the number of DGNSS measurements; (c) The triangular chart of integrity monitoring based on the Principal Gaussian overbound; (d) The triangular chart of integrity monitoring based on the two-step Gaussian overbound.

the sigma inflation will change the parameters of the original PGO, which makes the analysis complicated.

The PGO is determined by four parameters, including σ_1, σ_2, p_1, and the core-tail transition point x_{rp}, where σ_1, σ_2, and p_1 are determined by the fitted BGMM, and x_{rp} is determined by the partition parameter α, which needs to be specified. Fig. 11a plots the PGO of the 1-month CORS DGNSS errors ($30° \sim 35°$) with different settings of α in terms of CCDF. It is impressive that the overbounding results are almost the same regardless of the change of α. In (29), α can be interpreted as the threshold for the relative error between the kurtosis of the truncated BGMM and the truncated standard normal distribution. When the relative kurtosis error at the intersection point of $s_1(x)$ and $s_2(x)$ is very small (even smaller than α), the core-tail transition point will be set as the intersection point, as indicated by the first line of (29). Since the CORS DGNSS error ($30° \sim 35°$) is slightly heavy-tailed, its core part is almost Gaussian distributed. Therefore, the relative kurtosis error at the intersection point of $s_1(x)$ and $s_2(x)$ is very small. As a result, the core-tail transition point will be set as the intersection point of $s_1(x)$ and $s_2(x)$ regardless of the change of α, which completely determines the parameters of the PGO. Therefore, different α yields almost the same overbounding results, as observed in Fig. 11a.

The situation in the urban DGNSS error bounding is different. The PGO for urban DGNSS errors ($30° \sim 35°$) with different settings of α is plotted in Fig. 11b. The

CDF plot is chosen instead of the CCDF plot because the left tail of the urban DGNSS error is much heavier than the right tail, as shown in Fig. 9a. From Fig. 11b, it is observed that the change in the bounding performance of the PGO has two stages: In the first stage ($\alpha \leq 0.14$), the tail of PGO becomes sharper with the increase of α; In the second stage ($\alpha > 0.14$), the tail of PGO almost ceases to change with the increasing α. The changing pattern in the first stage can be attributed to the significant heavy-tailedness of the urban DGNSS error distribution, which leads to a significant heavy tail of the fitted BGMM. Therefore, the relative kurtosis error is extremely large at the intersection point of $s_1(x)$ and $s_2(x)$. When α takes a smaller value than the relative kurtosis error at the intersection point, the core-tail transition point will be purely determined by α, as shown in the second line of (29). Under this condition, the increase of α will push the core-tail transition point to the far end (but not as far as the core-tail transition point), which can be easily observed in Fig. 11b. However, when α becomes too large and enters the second stage, the relative kurtosis error at the intersection point will be smaller than α. As a result, the core-tail transition point will be set as the intersection point of $s_1(x)$ and $s_2(x)$ regardless of the change of α, which explains the pattern in the second stage. The thumbnail in Fig. 11b shows the bounding conditions in the region $[-3.3\,\mathrm{m}, -2.6\,\mathrm{m}]$. When α is larger than 0.06, the number of unbounded samples increases with the increase in α. This could be explained by the fact that
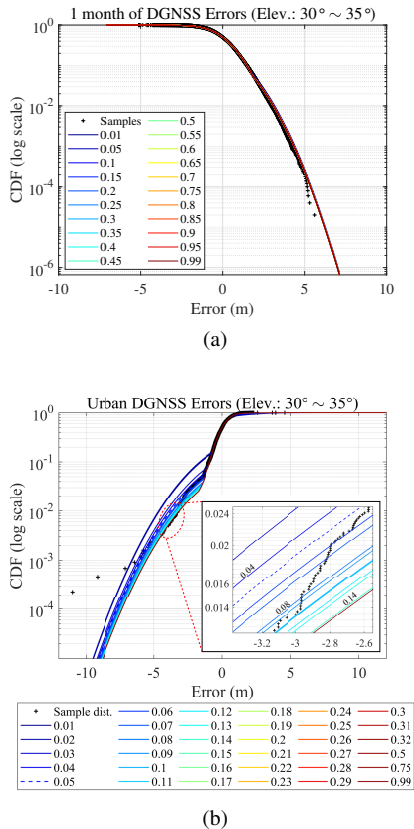
(a)

(b)

Fig. 11. The Principal Gaussian overbound (without sigma inflation) of (a) 1-month CORS DGNSS errors; and (b) urban DGNSS errors for elevation angles observed from $30°$ to $35°$.

the 2nd Gaussian component has an increasing impact on the core region with the increasing α, as illustrated in Section IV.B. In this case, the sigma inflation has to be implemented to ensure that the PGO can bound the sample distribution. However, the sigma inflation strategy unavoidably increases the conservatism of the PGO. Therefore, when bounding errors with significantly heavy tails, a small α is preferred to partition the core and tail regions. In this study, we take $\alpha = 0.05$ in the urban DGNSS experiments, which realize a good balance of dominance partition and overbounding.

B. Mean Bias Problems

The proposed PGO assumes that the error distribution has a zero mean, which is valid under open-sky conditions but may not always hold in urban areas due to non-line-of-sight (NLOS) and multipath. Therefore, this section discusses the effects of non-zero mean on the bounding results of the proposed PGO, intuitively illustrating the inapplicable situations for the proposed approach.

As shown in the histogram in Appendix I, the urban DGNSS error for elevation angles observed from $40°$ to $45°$ has a mean value of $-0.26\,\mathrm{m}$, which is taken for further analysis. Fig. 12 shows the Principal Gaussian overbounds before and after sigma inflation of the error distribution. The sigma inflation is designed to stop early

at the 50th iteration. As can be seen, the PGO without sigma inflation fails to bound the entire left region of errors, while the PGO with sigma inflation fails to bound the left-core region ($-0.5 \sim 0$ m). Although we can keep inflating the PGO with more iterations in Algorithm 1, the overbounding condition will not be satisfied. This could be explained by some derivations as the following. According to (39c), $G_o^{\mathrm{core}}(0) = 0.5$. Since CDF is a monotonically increasing function, we have

$$G_o^{\mathrm{core}}(x) < G_o^{\mathrm{core}}(0) = 0.5, \forall x < 0. \tag{83}$$

Denote $G(x)$ as the CDF of the error distribution in Fig. 12. Assume $G(x^*) = 0.5$, and then it is obvious that $x^* < 0$. Therefore,

$$G_o^{\mathrm{core}}(x^*) < G(x^*), \tag{84}$$

indicating that the bounding condition at the left region of errors is violated. Therefore, the proposed method is theoretically inapplicable to error distributions with non-zero mean. The results in Fig. 12 provide an intuitive example of the limitations of the proposed method.
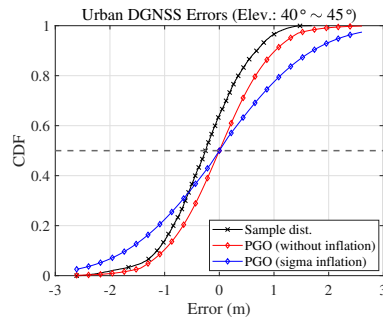

Fig. 12. The CDF of the PGO for urban DGNSS errors for elevation angles observed from $40°$ to $45°$. Since the overbounding conditions cannot be satisfied, the sigma inflation is designed to stop early at the 50th iteration.

C. Opportunities in Fault Detection

Ensuring a unified distribution that encompasses fault detection, overbounding, and PL calculation is crucial for integrity monitoring. To the authors' best knowledge, the Gaussian distribution is the sole viable option for implementing this harmonized framework. However, the PGO proposed in this study holds the potential to emerge as a compelling alternative. The bounding performance of the PGO in both range and position domains is already illustrated in Section V. In this section, we briefly discuss the feasibility of employing the PGO for fault detection.

One of the most straightforward approaches would be the maximum solution separation algorithm [34]–[36]. Since the maximum solution separation is a linear combination of measurement errors, its distribution can be obtained by taking convolutions if the measurement errors are assumed to be mutually independent. The detection threshold is given by the quantile of the distribution of the maximum solution separation. Furthermore, the computation load can be reduced by using the fast Fourier

transform to replace convolution operations, as shown in (73). Other approaches geared toward Gaussian distributed errors, such as the Chi-squared test [1], [37], [38], are not so straightforward to apply. However, the PGO has an explicit distribution, which potentially provides the theoretical foundation to conduct statistical analysis and hypothesis tests. The development of fault detection algorithms based on the PGO goes beyond the scope of this paper and will be considered in our future work.

VII. CONCLUSIONS

This study proposes the PGO for bounding heavy-tailed error distribution. Specifically, the BGMM is employed to fit the error distribution based on the EM algorithm. The CDF overbound of the BGMM is constructed based on the dominant relationship of each Gaussian component at the core and the tail region of the BGMM, respectively. In addition, a sigma inflation strategy is proposed to compensate the PGO, which allows it to bound the sample distribution as well as the fitted BGMM. The overbounding property is proven to be preserved through convolution, which makes it possible to derive pseudorange-level requirements from the position domain integrity requirements. The experimental results on the CORS and urban datasets show that the PGO provides the most competitive bounding performance for heavy-tailed DGNSS error, yielding a sharp bound in the core part of the error distribution. Compared to the two-step Gaussian overbounding method, the proposed method reduces the mean VPL by more than 78% without compromising integrity on the urban dataset. In addition, the computation load of calculating VPL is reduced by employing the fast Fourier transform, where the mean computation time is only $0.08\,\mathrm{s}$ with fifteen measurements. These results suggest the substantial potential of the PGO in GNSS applications with strict integrity and real-time requirements.

Although the PGO demonstrates promising bounding performance for heavy-tailed distributions, it does possess limitations when confronted with biases in error distributions. This issue is non-trivial, particularly within the context of GNSS error bounding. Possible solutions include employing paired overbounding methods and introducing bias terms to the BGMM. However, it is necessary to conduct a thorough analysis of the property of convolution preservation to ensure that these modifications are applicable for integrity applications, which will be the main focus of our future research.

Appendix A
The EM algorithm

The PDF of a K-component GMM model with mixture weights of p_1, p_2,..., p_K can be written as

$$f\left(x\mid\Theta\right) = \sum_{k=1}^{K} p_k f_N\left(x; b_k, \sigma_k\right), \qquad (85)$$

where Θ represents all parameters, including each Gaussian component's mixture weight, mean, and variance. For a given observation x_i, we define the allocation (latent) variable $c = \{1, 2, \ldots, K\}$ that marks the Gaussian component from which x_i is generated. Then, the mixture weight of Gaussian components can be interpreted as the prior probability of the allocation variable as follows,

$$p_k = P\left(c = k\right). \qquad (86)$$

The membership weight of the GMM can be defined based on Bayes' Theorem as follows,

$$\begin{aligned} w_{i,k} &= P\left(c = k | x_i\right) \\ &= \frac{p_k f_N\left(x_i; b_k, \sigma_k\right)}{\sum_{k=1}^{K} p_k f_N\left(x_i; b_k, \sigma_k\right)}, \end{aligned} \qquad (87)$$

which indicates the posterior probability of a data point x_i being generated from the kth Gaussian component. The log-likelihood function can be written as

$$L\left(x|\Theta\right) = \sum_{i=1}^{N} \ln \sum_{k=1}^{K} P\left(x_i | c = k, b_k, \sigma_k\right) P\left(c = k\right). \qquad (88)$$

By utilizing Jensen's inequality [39], the above equation can be simplified as

$$L\left(x|\Theta\right) \geq Q\left(x|\Theta\right), \qquad (89a)$$

$$\begin{aligned} Q\left(x|\Theta\right) &= \sum_{i=1}^{N} \sum_{k=1}^{K} w_{i,k} \ln \frac{p_k f_N\left(x_i; b_k, \sigma_k\right)}{w_{i,k}} \\ &= \sum_{i=1}^{N} \sum_{k=1}^{K} w_{i,k} \left(\ln p_k - \frac{(x_i - b_k)^2}{2\sigma_k^2} \right. \\ &\quad \left. - \ln w_{i,k} - \ln \sqrt{2\pi\sigma_k^2} \right), \end{aligned} \qquad (89b)$$

where $Q\left(x|\Theta\right)$ is the lower bound of $L\left(x|\Theta\right)$. Therefore, the model parameters of GMM can be estimated by maximizing $Q\left(x|\Theta\right)$, which can be effectively achieved by the EM algorithm [16]. The EM algorithm is an iterative supervised training algorithm consisting of two steps: the E-step and the M-step. Firstly, the model parameters are randomly initialized. In the E-step, the algorithm calculates the value of membership weight $w_{i,k}$ based on the latest model parameters, as shown in (87). In the M-step, the algorithm updates the model parameters based on the value of $w_{i,k}$. In this step, the log-likelihood function is maximized by taking the partial derivative over the model parameters Θ and letting the partial derivative equal to zero. The two steps are repeated until convergence is reached.

Appendix B
PROOF OF TAIL REGION OVERBOUND

Recall that Section IV.C constructs the overbound distribution in the left-tail region as follows:

$$G_o^{\mathrm{L}}(x) = (1 + k)(1 - p_1) G(x; 0, \sigma_2) \ \forall x < x_{lp}. \qquad (90)$$

The difference between $G_o^{\mathrm{L}}(x)$ and $G(x)$ is given by

$$G_o^{\mathrm{L}}(x) - G(x) = k(1 - p_1) G(x; 0, \sigma_2) - p_1 G(x; 0, \sigma_1). \qquad (91)$$

By substituting (35) into (91),

$$G_o^{\mathrm{L}}(x) - G(x) = \frac{p_1}{G\left(x_{lp}; 0, \sigma_2\right)} \Big(G\left(x_{lp}; 0, \sigma_1\right) G\left(x; 0, \sigma_2\right)$$
$$- G\left(x; 0, \sigma_1\right) G\left(x_{lp}; 0, \sigma_2\right) \Big). \tag{92}$$

If $G_o^{\mathrm{L}}(x)$ is the CDF overbound of $G(x)$, then the right-hand side of (92) should be non-negative, which is equivalent to prove

$$\frac{G\left(x_{lp}; 0, \sigma_1\right)}{G\left(x_{lp}; 0, \sigma_2\right)} > \frac{G\left(x; 0, \sigma_1\right)}{G\left(x; 0, \sigma_2\right)} \ \forall x < x_{lp}. \tag{93}$$

Let $f(x) = \frac{G(x; 0, \sigma_1)}{G(x; 0, \sigma_2)}$, then the derivative of $f(x)$ is given by

$$f^{'}(x) = \frac{f_N\left(x; 0, \sigma_1\right) G\left(x; 0, \sigma_2\right) - f_N\left(x; 0, \sigma_2\right) G\left(x; 0, \sigma_1\right)}{G^2\left(x; 0, \sigma_2\right)}. \tag{94}$$

Define

$$m\left(\sigma; x\right) = \frac{f_N\left(x; 0, \sigma\right)}{G\left(x; 0, \sigma\right)} = \frac{\frac{1}{\sigma\sqrt{2\pi}}\exp\left(-\frac{x^2}{2\sigma^2}\right)}{\frac{1}{2}\left[1 + \mathrm{erf}\left(\frac{x}{\sigma\sqrt{2}}\right)\right]} \tag{95a}$$

$$\forall \sigma > 0, x < x_{lp},$$

$$h\left(\gamma; x\right) = m\left(-\frac{1}{\gamma}; x\right) \ \forall \gamma < 0, x < x_{lp}. \tag{95b}$$

Then $h\left(\gamma; x\right)$ can be written as

$$h\left(\gamma; x\right) = \frac{\frac{\gamma}{-\sqrt{2\pi}}\exp\left(-\frac{\gamma^2}{2\left(-\frac{1}{x}\right)^2}\right)}{\frac{1}{2}\left[1 + \mathrm{erf}\left(\frac{\gamma}{\left(-\frac{1}{x}\right)\sqrt{2}}\right)\right]}$$

$$= \frac{\frac{\gamma}{x} \cdot \frac{1}{\left(-\frac{1}{x}\right)\sqrt{2\pi}}\exp\left(-\frac{\gamma^2}{2\left(-\frac{1}{x}\right)^2}\right)}{\frac{1}{2}\left[1 + \mathrm{erf}\left(\frac{\gamma}{\left(-\frac{1}{x}\right)\sqrt{2}}\right)\right]} \tag{96}$$

$$= \frac{1}{x} \cdot \gamma \frac{f_N\left(\gamma; 0, \left(-\frac{1}{x}\right)^2\right)}{G\left(\gamma; 0, -\frac{1}{x}\right)}.$$

Define $\lambda(\gamma) = \frac{f_N\left(\gamma; 0, \left(-\frac{1}{x}\right)\right)}{G\left(\gamma; 0, -\frac{1}{x}\right)}$, which is known as the inverse Mills ratio [40] and has the following properties [41]:

$$\lambda(\gamma) \geq 0 \ \forall \gamma \tag{97a}$$

$$\lambda^{'}(\gamma) < 0 \ \forall \gamma. \tag{97b}$$

Then the partial derivative of $h\left(\gamma; x\right)$ with respect to γ can be calculated as

$$\frac{\partial h\left(\gamma; x\right)}{\partial \gamma} = \frac{1}{x}\left[\lambda(\gamma) + \gamma\lambda^{'}(\gamma)\right]. \tag{98}$$

According to the chains rule,

$$\frac{\partial m\left(\sigma; x\right)}{\partial \sigma} = \frac{\partial h\left(-\frac{1}{\sigma}; x\right)}{\partial \sigma} = \frac{\partial h\left(-\frac{1}{\sigma}; x\right)}{\partial \gamma} \cdot \frac{\partial\left(-\frac{1}{\sigma}\right)}{\partial \sigma}$$
$$= \frac{1}{x}\left[\lambda\left(-\frac{1}{\sigma}\right) - \frac{1}{\sigma}\lambda^{'}\left(-\frac{1}{\sigma}\right)\right]\frac{1}{\sigma^2}. \tag{99}$$

When $x < 0$, we can easily prove that $\frac{\partial m(\sigma; x)}{\partial \sigma} < 0$. This means that $m\left(\sigma; x\right)$ is a monotonically decreasing function when $x < 0$. Therefore,

$$m\left(\sigma_1; x\right) = \frac{f_N\left(x; 0, \sigma_1\right)}{G\left(x; 0, \sigma_1\right)} > \frac{f_N\left(x; 0, \sigma_2\right)}{G\left(x; 0, \sigma_2\right)}$$
$$= m\left(\sigma_2; x\right) \ \forall \sigma_2 > \sigma_1 > 0, x < 0. \tag{100}$$

This is equivalent to saying that (94) has the property as follows:

$$f^{'}(x) > 0 \ \forall \sigma_2 > \sigma_1 > 0, x < 0. \tag{101}$$

Equation (101) indicates that $f(x)$ is a monotonically increasing function when $x < 0$, and therefore (93) is proved. Then, we can conclude that $G_o^{\mathrm{L}}(x)$ is the CDF overbound of $G(x)$ when $x < x_{lp}$. According to the symmetric property of $G_o^{\mathrm{L}}(x)$ and $G_o^{\mathrm{R}}(x)$, $G_o^{\mathrm{R}}(x)$ is easy to be proved as the CDF overbound of $G(x)$ when $x > x_{rp}$. This ends the proof.

Appendix C
PROOF OF MONOTONICITY

In the PGO, its PDF discontinues at the core-tail transition points x_{lp} and x_{rp}. The value of the leap at x_{lp} can be written as

$$f_o^{\mathrm{core}}\left(x_{lp}\right) - f_o^L\left(x_{lp}\right)$$
$$= -\left(1 + k\right)\left(1 - p_1\right) f_N\left(x_{lp}; 0, \sigma_2\right) \tag{102}$$
$$+ p_1 f_N\left(x_{lp}; 0, \sigma_1\right) + c.$$

Define

$$k^* = \frac{p_1 f_N\left(x_{lp}; 0, \sigma_1\right)}{\left(1 - p_1\right) f_N\left(x_{lp}; 0, \sigma_2\right)}. \tag{103}$$

As proved in (100) in Appendix B,

$$\frac{f_N\left(x; 0, \sigma_1\right)}{G\left(x; 0, \sigma_1\right)} > \frac{f_N\left(x; 0, \sigma_2\right)}{G\left(x; 0, \sigma_2\right)} \ \forall \sigma_2 > \sigma_1 > 0, x < 0. \tag{104}$$

We have

$$k^* = \frac{p_1 f_N\left(x_{lp}; 0, \sigma_1\right)}{\left(1 - p_1\right) f_N\left(x_{lp}; 0, \sigma_2\right)}$$
$$> \frac{p_1 G\left(x_{lp}; 0, \sigma_1\right)}{\left(1 - p_1\right) G\left(x_{lp}; 0, \sigma_2\right)} \tag{105}$$
$$= k > 0 \quad \forall \sigma_2 > \sigma_1 > 0, x < 0.$$

Therefore,

$$f_o^{\mathrm{core}}\left(x_{lp}\right) - f_o^{\mathrm{L}}\left(x_{lp}\right)$$
$$> -\left(1 + k^*\right)\left(1 - p_1\right) f_N\left(x_{lp}; 0, \sigma_2\right) \tag{106}$$
$$+ p_1 f_N\left(x_{lp}; 0, \sigma_1\right) + c.$$

Substituting (40) and (103) into (106), we have

$$f_o^{\mathrm{core}}\left(x_{lp}\right) - f_o^{\mathrm{L}}\left(x_{lp}\right) > \frac{1 - p_1}{x_{lp}}\Big(G\left(x_{lp}; 0, \sigma_2\right)$$
$$- x_{lp} f_N\left(x_{lp}; 0, \sigma_2\right) - 0.5\Big). \tag{107}$$

Define

$$g\left(x_{lp}\right) = G\left(x_{lp}; 0, \sigma_2\right) - x_{lp} f_N\left(x_{lp}; 0, \sigma_2\right) - 0.5, \tag{108}$$

then its first derivative can be calculated as

$$g^{'}\left(x_{lp}\right) = \left(1 + \frac{x_{lp}^2}{\sigma_2^2}\right) f_N\left(x_{lp}; 0, \sigma_2\right) > 0. \tag{109}$$

Since $g(0) = 0$, we have

$$g\left(x_{lp}\right) < 0 \ \forall x_{lp} < 0. \tag{110}$$

Therefore, (107) can be written as

$$f_o^{\mathrm{core}}\left(x_{lp}\right) - f_o^{\mathrm{L}}\left(x_{lp}\right) > \frac{1 - p_1}{x_{lp}} g\left(x_{lp}\right) > 0 \quad \forall x_{lp} < 0. \tag{111}$$

Since

$$f_o^{L'}(x) = -\frac{x}{\sigma_2^2}(1+k)\,p_2 f_N(x;0,\sigma_2) > 0 \quad \forall x < x_{lp} \quad (112a)$$

$$f_o^{core'}(x) = -\frac{x}{\sigma_1^2}p_1 f_N(x;0,\sigma_1) > 0 \quad \forall x_{lp} < x < 0, \quad (112b)$$

we can conclude that $f_o(x)$ is a monotonically increasing function when $x < 0$.

Appendix D
PROVE TO EQUATION (62)

Let $Y_i = s_{3,i}\Delta\rho_i$ be a new random variable. The CDF of Y_i is given by

$$F_{Y_i}(y) = P(Y_i < y) = P\left(\Delta\rho_i < \frac{y}{|s_{3,i}|}\right)$$
$$= \int_{-\infty}^{y/|s_{3,i}|} f_{r_i}(x)\,\mathrm{d}x. \quad (113)$$

Let $t = |s_{3,i}|\,x$, then we have

$$F_{Y_i}(y) = \frac{1}{|s_{3,i}|}\int_{-\infty}^{y} f_{r_i}\left(\frac{t}{|s_{3,i}|}\right)dt. \quad (114)$$

Appendix E
IMPACTS OF SAMPLE INTERVAL

To investigate the impacts of T on the position error bounding performance, we choose different T, including $0.01\,\mathrm{m}$, $0.05\,\mathrm{m}$, $2\,\mathrm{m}$, $5\,\mathrm{m}$, and $10\,\mathrm{m}$, to calculate the VPL for the vertical positioning error in urban DGNSS experiment. In each setting, we keep $T \times L = 30$, which is the value of x_{2L-1}. For example, in the setting of $T = 0.05\,\mathrm{m}$, L should be 600. Fig. 13 shows the time series of VPE produced by the DGNSS positioning method. The VPL calculated based on the PGO with different T is also plotted for comparison. The VPL gradually increases with the increase in T, as expected. This is because a large T would result in an over-conservative discrete overbound for $F_{o,Y_i}[n]$, which consequently increases the VPL. In addition, we notice that the VPL with $T = 0.01\,\mathrm{m}$ and $T = 0.05\,\mathrm{m}$ are almost the same, which means there is little room to reduce the VPL by reducing T when T is already less than $0.01\,\mathrm{m}$.
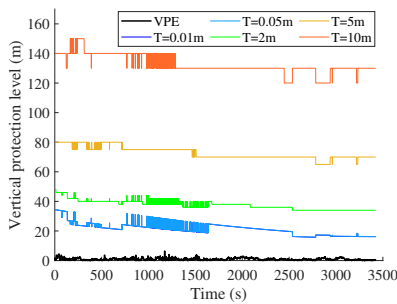

Fig. 13. The time series of VPE and VPL based on the Principal Gaussian overbound with different settings of T. $P_{\mathrm{HMI}} = 10^{-9}$.

Appendix F
SIGMA INFLATION ALGORITHM

Algorithm 1 shows the pseudocode of the sigma inflation algorithm.

Algorithm 1 Sigma Inflation

Input:
    Empirical CDF of Samples: $G_n(x)$
    Parameters of the before-inflation PGO: p_1, σ_1, σ_2, x_{lp}, x_{rp}
Output:
    Inflated sigma: σ_1^*, σ_2^*
1: Initialize the inflation factor: $\tau_1 = 1.01$, $\tau_2 = 1.01$
2: Core condition: $\Xi_{core} \leftarrow G_o^{core}(x) \geq G_n(x)\ \forall x_{lp} < x < 0$ AND $G_o^{core}(x) \leq G_n(x)\ \forall 0 < x < x_{rp}$
3: Tail condition: $\Xi_{tail} \leftarrow G_o^L(x) \geq G_n(x)\ \forall x \leq x_{lp}$ AND $G_o^R(x) \leq G_n(x)\ \forall x \geq x_{rp}$
4: **while** Ξ_{core} is false OR Ξ_{tail} is false **do**
5:     **if** Ξ_{core} is false **then**
6:         $\sigma_1 \leftarrow \tau_1 * \sigma_1$
7:     **end if**
8:     Update the tail condition Ξ_{tail} with the latest PGO parameter
9:     **if** Ξ_{tail} is false **then**
10:         $\sigma_2 \leftarrow \tau_2 * \sigma_2$
11:         $\sigma_1 \leftarrow$ (50)
12:     **end if**
13:     Update the core condition Ξ_{core} with the latest PGO parameter
14:     Update the tail condition Ξ_{tail} with the latest PGO parameter
15: **end while**
16: $\sigma_1^* \leftarrow \sigma_1$, $\sigma_2^* \leftarrow \sigma_2$

Appendix G
STEPS FOR IMPLEMENTING PRINCIPAL GAUSSIAN OVERBOUND

Algorithm 2 shows the implementation of the Principal Gaussian overbound.

Algorithm 2 Implementation of Principal Gaussian Overbound

Input:
    Error data: $X = \{x_1, x_2, \cdots, x_n\}$
    Partition parameter: α
Output:
    Parameters of PGO: p_1, σ_1^*, σ_2^*, x_{lp}, x_{rp}
1: Fit a BGMM
    $f(x) = p_1 f_N(x;0,\sigma_1) + (1-p_1)f_N(x;0,\sigma_2)$
    $\leftarrow$ Employ EM algorithm with X
2: $x_{lp}, x_{rp} \leftarrow$ Dominance partition by (29), (30)
3: $k \leftarrow$ Calculate the scaling parameter by (35)
4: $c \leftarrow$ Calculate the shifting parameter by (40)
5: $\sigma_1^*, \sigma_2^* \leftarrow$ Algorithm 1 with p_1, σ_1, σ_2, x_{lp}, x_{rp}

Appendix H
PARAMETERS OF THREE METHODS

TABLE II
Parameters of the Principal Gaussian, two-step Gaussian, and Gaussian-Pareto overbounding methods on different datasets

	Dataset name	CORS DGNSS	CORS DGNSS	CORS DGNSS	Urban DGNSS
Datasets	Time Span	1 month	1 year	1 year	57 minutes
	Elevation angle	$30° \sim 35°$	$30° \sim 35°$	$60° \sim 65°$	$30° \sim 35°$
	No. of samples	49,779	602,724	322,462	4,324
Principal Gaussian	σ_1	0.965	0.984	0.678	0.817
	σ_2	1.820	1.992	1.091	3.811
	p_1	0.635	0.696	0.794	0.900
	x_{rp}	1.751	1.983	1.654	1.653
Two-step Gaussian	$(b_\mathrm{L}, b_\mathrm{R})$	$(0.168, 0.168)$	$(0.188, 0.188)$	$(0.021, 0.021)$	$(2.895, 2.895)$
	$(\sigma_\mathrm{L}, \sigma_\mathrm{R})$	$(1.751, 1.751)$	$(1.898, 1.898)$	$(1.035, 1.035)$	$(3.351, 3.351)$
Gaussian Pareto	σ_GP	1.251	1.557	0.869	0.954
	$(u_\mathrm{L}, u_\mathrm{R})$	$(-1.780, 2.006)$	$(-3.813, 4.893)$	$(-1.284, 1.408)$	$(-1.003, 1.126)$
	$(\gamma_\mathrm{L}, \gamma_\mathrm{R})$	$(-0.063, -0.052)$	$(0.022, 0.086)$	$(-0.036, -0.007)$	$(0.204, 0.307)$
	$(\beta_\mathrm{L}, \beta_\mathrm{R})$	$(0.579, 0.646)$	$(0.349, 0.598)$	$(0.384, 0.387)$	$(0.795, 0.257)$

Appendix I
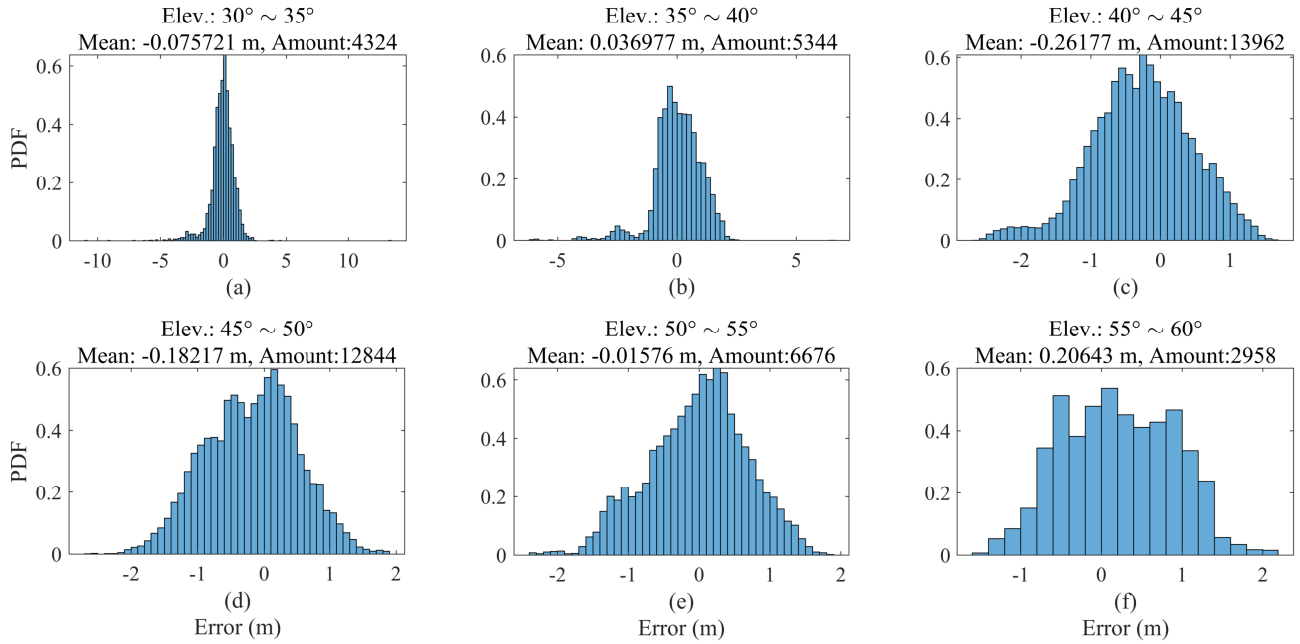## DISTRIBUTION OF THE URBAN DATASET

Fig. 14. The histogram of the urban DGNSS error with the SNR larger than $35\,\mathrm{dB}$ and the elevation angle larger than $30°$ in each $5°$ elevation angle bin. The mean value of the DGNSS error and the amount of samples in each bin are presented in the title of each subplot. The bins with less than 5 samples are not plotted.

Appendix J
ADDITIONAL BOUNDING RESULTS OF URBAN DGNSS ERRORS

Fig. 15 shows the bounding results of urban DGNSS errors for elevation angles observed from $35°$ to $40°$. Similar to the results in Section V.C.2, the PGO still yields a considerably tight bound in the core region and shows moderate overall bounding performance among the three overbounding methods. Fig. 16 shows the bounding results of urban DGNSS errors for elevation angles observed from $50°$ to $55°$, where the sample distribution is not significantly heavy-tailed. Similar to the bounding results of CORS DGNSS error with high elevation angles ($60° \sim 65°$) in Section V.B.2, the three overbounding methods show slight difference. Therefore, the Gaussian overbound is recommended due to its simplicity.
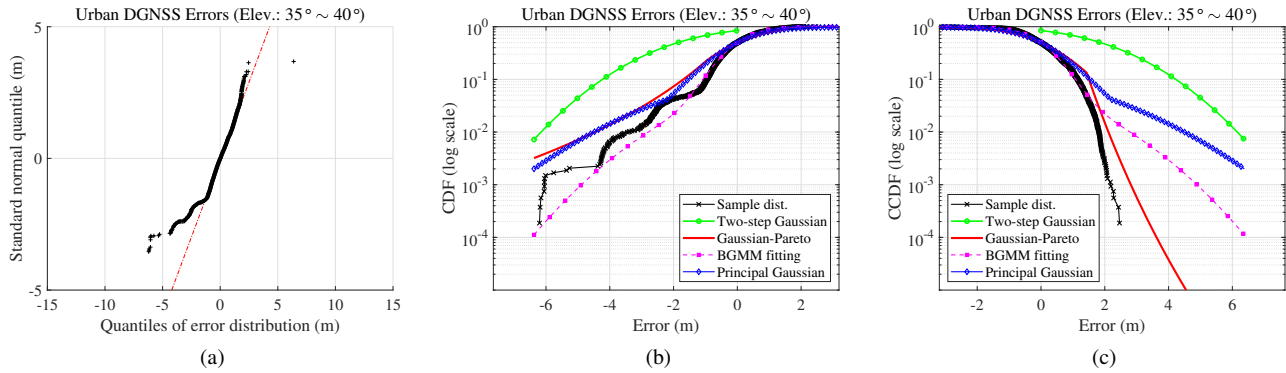

Fig. 15. (a) The QQ plot of urban DGNSS errors for elevation angles observed from $35°$ to $40°$; and the distribution of three overbounding methods in two views: (b) CDF plotted on a logarithmic scale; (c) CCDF plotted on a logarithmic scale, where "Two-step Gaussian (L)" and "Two-step Gaussian (R)" represent the two-step Gaussian overbound at the left region and the right region, respectively.
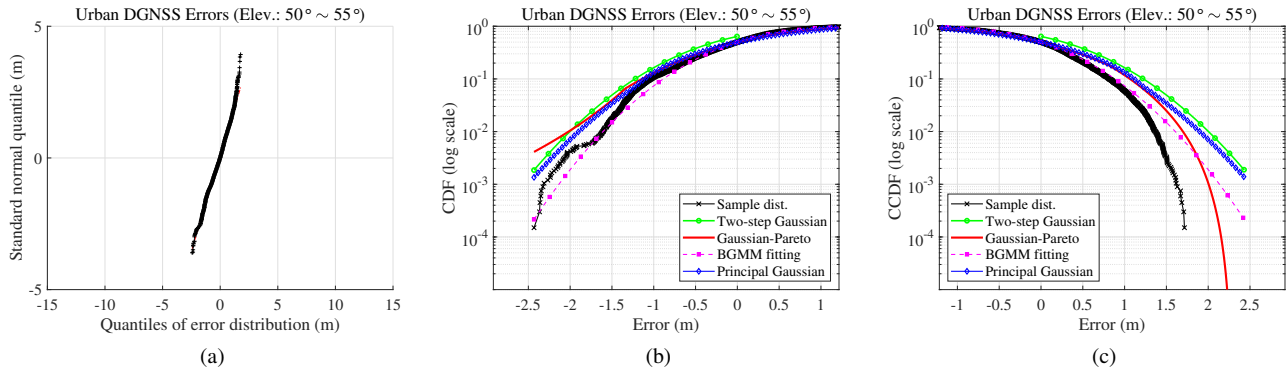

Fig. 16. (a) The QQ plot of urban DGNSS errors for elevation angles observed from $50°$ to $55°$; and the distribution of three overbounding methods in two views: (b) CDF plotted on a logarithmic scale; (c) CCDF plotted on a logarithmic scale, where "Two-step Gaussian (L)" and "Two-step Gaussian (R)" represent the two-step Gaussian overbound at the left region and the right region, respectively.
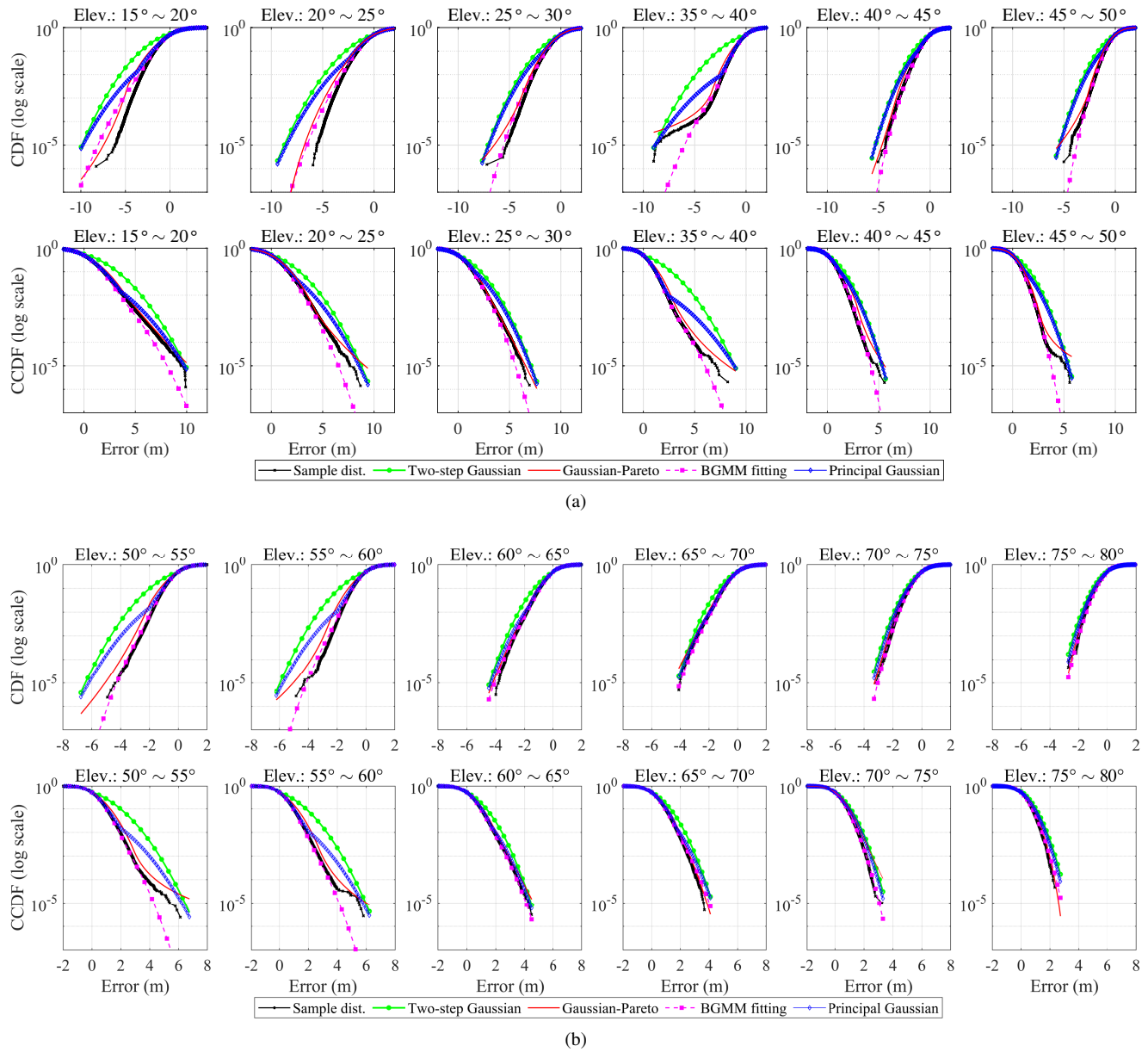
(a)

(b)

Fig. 17. Overbounding results for 1-year CORS DGNSS errors in each $5°$ elevation angle bin. The case of bin $30° \sim 35°$ is not present due to the space limit. One can refer to Fig. 5 for the results of bin $30° \sim 35°$. In addition, the results of bin $80° \sim 85°$ and $85° \sim 90°$ are not present because the number of samples in these bins is less than 1,300, which is less than the minimum requirement in the Gaussian-Pareto overbound.

REFERENCES

[1] T. Walter and P. Enge, "Weighted RAIM for precision approach," in *Proc. 8th Int. Tech. Meeting Satell. Division Inst. Navigat.*, Palm Springs, CA, Sep. 1995, pp. 1995–2004.

[2] R. G. Brown, "A Baseline GPS RAIM Scheme and a Note on the Equivalence of Three RAIM Methods," *Navig. J. Inst. Navig.*, vol. 39, no. 3, pp. 301–316, Sep. 1992. [Online]. Available: https://onlinelibrary.wiley.com/doi/10.1002/j.2161-4296.1992.tb02278.x

[3] F. C. Chan, M. Joerger, S. Khanafseh, and B. Pervan, "Bayesian fault-tolerant position estimator and integrity risk bound for gnss navigation," *J. Navig.*, vol. 67, no. 5, pp. 753–775, 2014.

[4] J. D. Larson, D. Gebre-Egziabher, and J. H. Rife, "Gaussian-Pareto overbounding of DGNSS pseudoranges from CORS," *Navig. J. Inst. Navig.*, vol. 66, no. 1, pp. 139–150, Jan. 2019.

[5] J. Rife, T. Walter, and J. Blanch, "Overbounding SBAS and GBAS Error Distributions with Excess-Mass Functions," in *Proc. Int. Symp. GPS/GNSS*, Sydney, Australia, 2004.

[6] R. Braff and C. Shively, "A method of over bounding ground based augmentation system (GBAS) heavy tail error distributions," *J. Navig.*, vol. 58, no. 1, pp. 83–103, 2005.

[7] C. A. Shively, "A Comparison of LAAS Error Bounding Concepts," in *Proc. Nat. Tech. Meeting Inst. Navigat.*, Long Beach, CA, Jan. 2001, pp. 501–511.

[8] J. Rife, S. Pullen, and B. Pervan, "Core Overbounding and its Implications for LAAS Integrity," in *Proc. 17th Int. Tech. Meeting Satell. Division Inst. Navigat.*, Long Beach, CA, Sep. 2004, pp. 2810–2821.

[9] B. DeCleene, "Defining Pseudorange Integrity - Overbounding," in *Proc. 13th Int. Tech. Meeting Satell. Division Inst. Navigat.*, Salt Lake City, UT, Sep. 2000, pp. 1916–1924.

[10] J. Blanch, T. Walter, and P. Enge, "Gaussian Bounds of Sample Distributions for Integrity Analysis," *IEEE Trans. Aerosp. Electron. Syst.*, vol. 55, no. 4, pp. 1806–1815, Aug. 2019.

[11] J. Rife, S. Pullen, B. Pervan, and P. Enge, "Paired overbounding and application to GPS augmentation," in *Proc. IEEE/ION Position Location Navigation Symp.*, Monterey, CA, USA, 2004, pp. 439–446. [Online]. Available: http://ieeexplore.ieee.org/document/1309027/

[12] J. Blanch, T. Walter, and P. Enge, "Position error bound calculation for GNSS using measurement residuals," *IEEE Trans. Aerosp. Electron. Syst.*, vol. 44, no. 3, pp. 977–984, Jul. 2008.

[13] T. Dautermann, C. Mayer, F. Antreich, A. Konovaltsev, B. Belabbas, and U. Kalberer, "Non-gaussian error modeling for gbas integrity assessment," *IEEE Trans. Aerosp. Electron. Syst.*, vol. 48, no. 1, pp. 693–706, 2012.

[14] R. Xue, Z. Wang, and Y. Zhu, "Upper bound estimation of positioning error for ground-based augmentation system," *GPS Solut.*, vol. 21, no. 4, pp. 1781–1790, Oct. 2017.

[15] Z. Gao, K. Fang, Z. Wang, K. Guo, and Y. Liu, "An Error Overbounding Method Based on a Gaussian Mixture Model with Uncertainty Estimation for a Dual-Frequency Ground-Based Augmentation System," *Remote Sens.*, vol. 14, no. 5, p. 1111, Feb. 2022.

[16] A. P. Dempster, N. M. Laird, and D. B. Rubin, "Maximum Likelihood from Incomplete Data Via the EM Algorithm," *J. R. Stat. Soc. B*, vol. 39, no. 1, pp. 1–22, Sep. 1977.

[17] H. J. Nussbaumer, *The Fast Fourier Transform*. Berlin, Heidelberg: Springer Berlin Heidelberg, 1982, pp. 80–111. [Online]. Available: https://doi.org/10.1007/978-3-642-81897-4_4

[18] J. Pickands III, "Statistical inference using extreme order statistics," *the Annals of Statistics*, pp. 119–131, 1975.

[19] S. Coles, *Threshold Models*. London: Springer London, 2001, pp. 74–91. [Online]. Available: https://doi.org/10.1007/978-1-4471-3675-0_4

[20] T. Walter, K. Gunning, R. Eric Phelts, and J. Blanch, "Validation of the unfaulted error bounds for araim," *Navig. J. Inst. Navig.*, vol. 65, no. 1, pp. 117–133, 2018.

[21] Y. Yun, H. Yun, D. Kim, and C. Kee, "A Gaussian sum filter approach for dgnss integrity monitoring," *J. Navig.*, vol. 61, no. 4, pp. 687–703, 2008.

[22] J. Lee, "LAAS Position Domain Monitor Analysis and Test Results for CAT II/III Operations," in *Proc. 17th Int. Tech. Meeting Satell. Division Inst. Navigat.*, Long Beach, CA, Sep. 2004, pp. 2786–2796.

[23] J. A. Rice, *Probability*. Thomson Brooks/Cole, 2007, p. 1–26.

[24] W. C. Horrace, "Moments of the truncated normal distribution," *Journal of Productivity Analysis*, vol. 43, pp. 133–138, 2015.

[25] S. Shah and M. Jaiswal, "Estimation of parameters of doubly truncated normal distribution from first four sample moments," *Annals of the Institute of Statistical Mathematics*, vol. 18, no. 1, pp. 107–111, 1966.

[26] O. Osechas and J. Rife, "Tightening DGNSS Protection Levels Using Direct Position-Domain Bounding," in *Proc. 26th Int. Tech. Meeting Satell. Division Inst. Navigat.*, Nashville, TN, Sep. 2013, pp. 1329–1340.

[27] Lee, Jiyun, S. Pullen, and P. Enge, "Sigma Overbounding using a Position Domain Method for the Local Area Augmentaion of GPS," *IEEE Trans. Aerosp. Electron. Syst.*, vol. 45, no. 4, pp. 1262–1274, Oct. 2009. [Online]. Available: http://ieeexplore.ieee.org/document/5310297/

[28] R. N. Bracewell, *The Fourier Transform and its Applications*, 3rd ed., ser. McGraw-Hill series in electrical and computer engineering. Boston: McGraw Hill, 2000.

[29] J. Rife and B. Pervan, "Overbounding revisited: Discrete error-distribution modeling for safety-critical GPS navigation," *IEEE Transactions on Aerospace and Electronic Systems*, vol. 48, no. 2, pp. 1537–1551, 2012.

[30] P. Misra and P. Enge, *Global Positioning System: Signals, Measurements, and Performance*, 2nd ed. Lincoln, Mass: Ganga-Jamuna Press, 2006.

[31] NASA. Broadcast ephemeris data. [Online]. Available: https://cddis.nasa.gov/Data_and_Derived_Products/GNSS/broadcast_ephemeris_data.html

[32] T. Takasu and A. Yasuda, "Development of the low-cost rtk-gps receiver with an open source program package RTKLIB," in *Proc. Int. Symp. GPS/GNSS*, vol. 1. International Convention Center Jeju Korea Seogwipo-si, Republic of Korea, 2009, pp. 1–6.

[33] SMO. Web download of satref gnss raw data. [Online]. Available: https://www.geodetic.gov.hk/en/rinex/downv.aspx

[34] R. G. Brown and P. W. McBurney, "Self-contained gps integrity check using maximum solution separation," *Navig. J. Inst. Navig.*, vol. 35, no. 1, pp. 41–53, 1988.

[35] B. W. Parkinson and P. Axelrad, "Autonomous GPS Integrity Monitoring Using the Pseudorange Residual," *Navig. J. Inst. Navig.*, vol. 35, no. 2, pp. 255–274, Jun. 1988. [Online]. Available: https://onlinelibrary.wiley.com/doi/10.1002/j.2161-4296.1988.tb00955.x

[36] M. Joerger, F.-C. Chan, and B. Pervan, "Solution Separation Versus Residual-Based RAIM," *Navig. J. Inst. Navig.*, vol. 61, no. 4, pp. 273–291, Dec. 2014. [Online]. Available: https://onlinelibrary.wiley.com/doi/10.1002/navi.71

[37] J. Blanch, T. Walter, and P. Enge, "RAIM with Optimal Integrity and Continuity Allocations Under Multiple Failures," *IEEE Trans. Aerosp. Electron. Syst.*, vol. 46, no. 3, pp. 1235–1247, Jul. 2010. [Online]. Available: http://ieeexplore.ieee.org/document/5545186/

[38] M. Joerger and B. Pervan, "Fault detection and exclusion using solution separation and chi-squared ARAIM," *IEEE Trans. Aerosp. Electron. Syst.*, vol. 52, no. 2, pp. 726–742, Apr. 2016. [Online]. Available: https://ieeexplore.ieee.org/document/7472967

[39] J. L. W. V. Jensen, "Sur les fonctions convexes et les inégalités entre les valeurs moyennes," *Acta Math.*, vol. 30, no. 1, pp. 175–193, 1906.

[40] J. P. Mills, "Table of the ratio: Area to bounding ordinate, for any portion of normal curve," *Biometrika*, pp. 395–400, Nov. 1926.

[41] W. Greene, *Econometric Analysis*, 4th ed. Upper Saddle River, NJ: Prentice Hall Internat, 2000.

Penggao Yan received the bachelor's degree in Communication Engineering in 2018 and the master's degree in Pattern Recognition and Intelligent Systems in 2021, both from Wuhan University, China. He is currently pursuing a Ph.D. degree at the Department of Aeronautical and Aviation Engineering, Faculty of Engineering, Hong Kong Polytechnic University.

His research interests include non-Gaussian noise modeling, fault detection and integrity monitoring in localization systems, and control-aided localization.

Yihan Zhong obtained his bachelor's degree in process equipment and control engineering from Guangxi University in 2020 and a Master's degree from The Hong Kong Polytechnic University (PolyU). He is currently a Ph.D. student at the Department of Aeronautical and Aviation Engineering, Faculty of Engineering, Hong Kong Polytechnic University.

His research interests include factor graph optimization-based collaborative positioning and low-cost localization.

Li-Ta Hsu (Senior Member, IEEE) received the B.S. and Ph.D. degrees in aeronautics and astronautics from National Cheng Kung University, Taiwan, in 2007 and 2013, respectively. He is currently an associate professor at the Department of Aeronautical and Aviation Engineering, Faculty of Engineering, Hong Kong Polytechnic University, before he served as a post-doctoral researcher in Institute of Industrial Science at University of Tokyo, Japan. In 2012, he was a visiting scholar in University College London, U.K. He is an Associate Fellow of RIN.

His research interests include GNSS positioning in challenging environments and localization for pedestrians, autonomous driving vehicles, and unmanned aerial vehicles.